Modified Fluid Closure of Weakly Collisional Plasmas in Radiatively-Inefficient Accretion Flows

Amelia Hankla

Advisor: James Stone. Second reader: Frans Pretorius

May 1, 2017

Abstract

The diversity of plasmas in nature divides their study into many different regimes which are valid only within certain approximations. This paper attempts to extend the validity of one such regime (a fluids framework) to another (kinetic theory, for collisionless plasmas). The focus is more narrowly on astrophysical systems, where studies of weakly collisional plasmas very often use the fluid model which should theoretically not apply. Recent kinetic simulations of black hole accretion flows make radiatively-inefficient accretion flows an ideal starting point to investigate the possibility of using a modified fluids closure to model weakly collisional plasmas. If the fluid regime is found to be an appropriate model, then the door is opened for future work on global simulations and other weakly collisional plasmas. Study of these accretion flows is done through three-dimensional local shearing box magnetohydrodynamic simulations with anisotropic viscosity and a maximum pressure anisotropy, a choice motivated by the aforementioned kinetic simulations.

Contents

This paper represents my own work in accordance with University
regulations.

Amelia Mary Hankla

Chapter 1

Introduction

1.1 Overview

The discipline of plasma physics encompasses a vast variety of plasmas, stretching from earthly laboratory-made fusion plasmas to astrophysical plasmas such as the intracluster medium and accretion flows onto compact objects. What separates this discipline into different subfields is the immense variety of scales in terms of distance, density, and temperature. Although the theory of magnetohydrodynamics is scale-less, the different relationship between parameters means that the plasma inside a tokamak is not usefully described by the same set of equations as a disk of matter around the black hole at the center of the galaxy, where the distances are tens of orders of magnitude greater, densities are tens of orders of magnitude times smaller, and temperatures ten times lower (see Table 1.1).

All plasmas can in principle be described by a collection of equations describing the Lorentz force and other interactions on every single particle in the plasma. As can easily be imagined, however, the task of following billions of particles is intractable both analytically and computationally. Different sets of assumptions allow the impossible equations to be reduced to something useful in their respective situations. For instance, plasmas in which the particles do not collide often if at all (termed "weakly collisional" or "col-

lisionless", respectively), need to be evolved using a distribution function that takes into account the spread of particle velocities: a kinetic theory. In contrast, when the particles in a plasma collide many times before they travel any meaningful distance in a system, the plasma can be treated as a fluid. Said fluid has only one "bulk" velocity at any given point. The fluid mechanical approach is thereby a simplification of the full kinetic theory. As such, we would not expect a fluid treatment of weakly collisional plasmas to hold much weight.

It is perhaps surprising then, that it is common practice to do so. This unjustified assumption is not so hard to understand given the conceptual and practical simplification that the fluids model presents: instead of evolving six degrees of freedom, there are only three. It is more intuitive to think about fluids as we have every day experience with them. Another reason is simply the inability to make progress otherwise: as late as 2011 fully-kinetic simulations were still "well beyond our present capability" [1]. So is the fluid assumption valid? To date an investigation of the validity of this assumption seems to be absent from the astrophysical literature, although similar works may exist in the fusion literature.

The main goal of this thesis is to explore the viability of modelling a weakly collisional plasma with a modified fluid closure. If such an approximation is found to exist, then the assumptions of past studies discussed below stand on firmer theoretical ground. The approximation would also pave the way for further studies of weakly collisional and collisionless plasmas, easing not only the conceptual difficulty of a full kinetic theory but also the computational nuisance of particle-in-cell (PIC) simulations, which are limited by the extreme amount of resources they consume (a PIC simulation that takes millions of cpu-hours can be done in tens to thousands of cpu-hours using a fluid model).

1.2 Collisionless and Weakly Collisional Plasmas

More formally, a collisionless plasma is one for which the particles on average travel longer than the scales one is interested in without colliding. This means that the length scale of interest L (the radius of an accretion disk, for example, or the distance between the sun and the earth for the solar wind) is much less than the mean free path λ_{mfp} of particles. In these cases the magnetic field is also strong enough such that the Larmor radius ρ is much less than both length scales of interest and the mean free path (a so-called "magnetized" plasma). We therefore have the ordering

$$\rho \ll \ L \ll \lambda_{mfp} \tag{1.1}$$

For weakly collisional plasmas, the mean free path is on the order of the length scales of interest: $\rho \ll L \sim \lambda_{mfp}$. These orderings are opposed to fluid models in which both the mean free path and the Larmor radius are much less than the length scales of interest ($\lambda_{mfp} \ll L, \rho \ll L$). The range of systems underneath the "collisionless" and "weakly collisional" plasma umbrella is still quite large and therefore worth studying. Collisionless plasmas are most typically found in the solar wind [2–4], while canonical weakly collisional plasmas are the intracluster medium between galaxies [5–7] and radiatively inefficient accretion flows (RIAFs) around black holes. Table 1.1 shows these collisionless and weakly collisional plasmas' parameters in comparison to collisional plasmas such as magnetically-confined fusion plasmas [8].

Radiatively-inefficient accretion flows (RIAFs) are often treated as a fluid, usually with qualifications about such *ad hoc* assumptions [9–16]. RIAFs are mainly found in two situations: binary systems and active galactic nuclei. Figure 1.1 shows illustrations of these two main regimes. Binary systems involve black holes on the order of tens of solar masses. In this regime it is hoped that the RIAF model can explain observations of x-ray binary outbursts, or transitions from the dormant quiescent soft state to the active hard state and vice versa [17–21] (other possible explanations include the

very complex phenomenon of black hole jets [22–24]; see [25] for a review). This thesis will concentrate on the other regime of RIAFs around supermassive black holes like Sagittarius A*, the one at the center of the galaxy.

Although other black holes like M87 [26–29] and GX 339-4 [30] have been studied, much of the literature focuses on Sagittarius A* due to its proximity. The accretion disk around this black hole is many times dimmer than one might expect, knowing that the gravitational energy of in-falling matter must go somewhere—and where does it go, if not into radiation that can then be detected on Earth? Current models suggest that the accretion disk is heated up, resulting in a hot flow whose mean free path between particles is correspondingly large: a weakly collisional plasma. Such flows are termed "radiatively inefficient accretion flows" (RIAFs) and are thought to effectively model low-luminosity active galactic nuclei (LLAGN) such as Sagittarius A* [1, 9, 31–33]. Models that accurately explain observations are becoming even more crucial as the Event Horizon Telescope probes ever closer to event horizon scales [34].
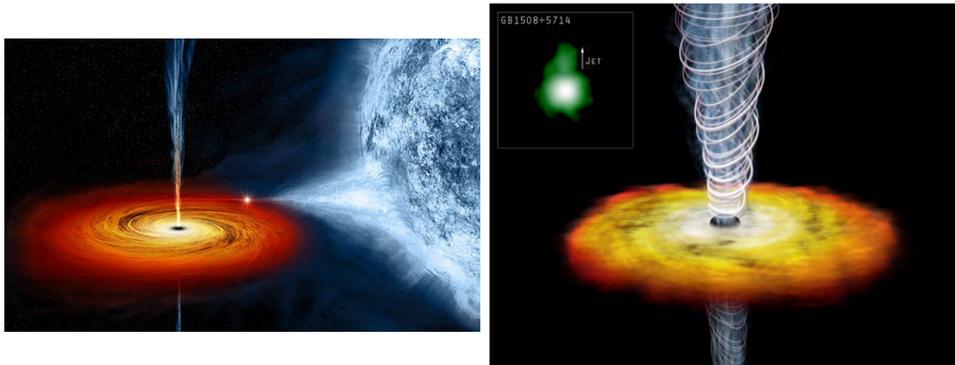
Figure 1.1: Artists' renderings of accretion disks. Left: accretion from a white dwarf onto a black hole. The accretion disk is in orange. Relativistic jets are shown launching out of the disk. Image from Luminet [35]. Right: around a supermassive black hole, supported by an image taken by the Chandra X-ray Observatory (inset). The disk itself is in orange, while magnetic field lines are shown in white around the collimated jets. Image from Siemiginowska and Weiss [36].

	L (cm)	n (cm^{-3})	T (eV)	B (G)	ρ (cm)	λ_{mfp} (cm)
ICM	6.2e23	5.0e-3	8.0e3	1.0e-6	1.3e10	9.5e21
RIAFs	3e17	1.0e2	2.0e3	1.0e-3	1e6	1e16
Solar wind	1.5e13	1.0e1	1.0e1	1.0e-4	4.6e6	1.2e13
ISM	3.1e20	1.0e0	1.0e0	5.0e-6	2.9e7	1.3e12
JET	1.0e2	1.0e14	1.0e4	3.0e4	4.8e-1	1.4e6

Table 1.1: Comparison of parameters of different plasmas found in space and on earth. ICM: intracluster medium. ISM: interstellar medium. JET: Joint European Torus (a tokamak). Collisionless and weakly collisional plasmas are above the horizontal lines; collisional plasmas are below. Numbers calculated from parameters given in Refs. [8, 37].

1.3 Motivation and Impacts

This thesis will concentrate on weakly collisional plasmas in the context of RIAFs. This choice is motivated both by a recent paper that presents the first kinetic simulation of how accretion in a RIAF happens locally [38] and by hints at the inability of a fluid model to capture the correct growth rates of kinetic phenomena [39]. Although there has been some study on modified fluid closures to capture kinetic physics [40–42] especially by Sharma et al. [43], henceforth referred to as Paper I, these studies use a different formalism and could only be compared to 2D simulations. Now that a 3D kinetic simulation has been performed by Kunz et al. [38], hereafter referred to as Paper II, a direct comparison between a modified fluid closure and kinetic theory is possible. The paper uses methods that are easily replicated using the Athena code developed by Stone et al. [44], in particular the same local shearing-box method [45]. A comparison is thus easily facilitated and meaningful.

This paper is complementary to other current research in the field of accretion disk physics that often assumes a high degree of collisionality: for example, the recent push to include general relativity in accretion disk calculations [20, 21, 26, 31, 46–52]. This thesis addresses the fundamental assumptions of these papers and assesses their validity, providing the ground-

work for extending magnetohydrodynamics to relativistic systems and other effects.

A fluid closure to kinetic physics has consequences beyond just black hole accretion. If proper parameters are found that sufficiently imitate the kinetic physics of RIAFs, then this model can be extended to global simulations and enables the exploration of the parameter space of other collisionless and weakly collisional plasmas. Such exploration is currently prohibitively expensive computationally because PIC simulations are required. If a fluid model is shown to reliably reproduce the same physics, then the simulations are much more manageable, allowing for more thorough scans of, for example, magnetic field strength. A fluid model closure to kinetic physics is also interesting in a conceptual sense since it would mean that the six phase-space degrees of freedom could be reduced to only three position-space degrees of freedom.

The structure of this paper is as follows: the necessary background to understand the fundamental plasma physics question and a brief history of the RIAF-related problem of accretion is outlined in Chapter 2. The actual physical mechanism for accretion, a linear MHD instability called the magnetorotational instability (MRI), is outlined in Chapter 3 using both analytic theory and the main tool of the rest of this thesis—simulations. Chapter 3 builds from the simplest (ideal) MHD theory to more complex, resistive MHD. Chapter 4 transitions into the original research of this thesis, using anisotropic viscosity along magnetic field lines in an attempt to capture kinetic physics with a modified fluid closure.

Chapter 2

Background

This chapter introduces the various plasma regimes and models for describing them in Section 2.1. Having chosen RIAFs as the context for the fundamental plasma physics problem, we then motivate the central problem of accretion in Section 2.2 and discuss previous studies of anisotropic viscosity in Section 2.3. The numerical codes in use are explained in Section 2.4. Equations are in Gaussian units unless otherwise specified.

2.1   Plasma Physics Regimes

Plasma physics applies to a wide range of subject areas, from magnetic-confinement fusion pursuits like the tokamak ITER [53] and the stellarator Wendelstein 7-X [54] to a variety of astrophysical situations, including the sun's corona and protoplanetary disks. The uniting theme across these different disciplines is the plasma: so what exactly is a plasma?

A plasma is the so-called "fourth state of matter", coming after the gas phase in the increasing kinetic energy hierarchy (solid-liquid-gas-plasma): that is, the inetic energy of a plasma particle is much greater than its potential energy. A plasma is made up of neutrals and the result of the neutrals' ionization: that is, ions and electrons. The basic physics of single-particle motion in electric and magnetic fields (for example, ∇B drift and

$E \times B$ drift) apply to every single particle. Given the enormous quantity of particles, working analytically or simulating such a situation for each individual particle is near impossible. Indeed, this is why the kinetic theory is so complicated and requires particle-in-cell simulations that use codes such as PEGASUS (Section 2.4). The task of this thesis is to make simulations feasible via (modified) fluid equations.

2.1.1 Characteristic Plasma Parameters

One parameter that will be frequently discussed (since it determines which model describes a plasma) is the mean free path λ_{mfp} of a plasma particle, that is, how far it travels on average before it collides with another particle. This is related to the thermal velocity $v_T = \sqrt{2T/m}$ and collision frequency $\omega_{coll} \sim nT^{-3/2}$ by

$$\lambda_{mfp} = \frac{v_T}{\omega_{coll}} \sim \frac{T^2}{n}\sqrt{\frac{2}{m}} \qquad (2.1)$$

where m is the mass of a particle of species with number density n. Notice that since the mass of an electron is so small compared to that of an ion (made up of protons and neutrons), the electron thermal velocity is much greater than the ion thermal velocity. This means that electrons are often fluid-like when ions are not.

An increase in temperature leads to an increase in the mean free path of a particle because it decreases the collision frequency. In general, a higher collision rate simplifies calculations [55]. This is because collisions push particles towards the Maxwell-Boltzmann (or Maxwellian) distribution of thermal equilibrium. Ideal MHD assumes a Maxwellian distribution. It is departures from this equilibrium that complicate calculations.

Now we turn to defining magnetization is plasmas, which is an important definition in Braginskii MHD. The most important parameter is the easily-derivable thermal gyroradius: $\rho_s \equiv v_{T_s}/\Omega_s$ where $\Omega_s = q_s B/m_s$ where q is the charge of a particle in magnetic field of strength B. A magnetized plasma

is one for which the dimensionless parameter $\delta \equiv \rho/L$ goes to zero. In this case, particles will follow orbits that oscillate many times about magnetic field lines as their guiding center travels along the field lines. In ideal MHD, both $\lambda_{mfp} \ll L$ and $\delta \ll 1$, whereas Braginskii MHD takes $\rho \ll \lambda_{mfp} \ll L$ and a weakly collisional plasma has $\lambda_{mfp} \gtrsim L$.

As will be explained more later, the balance of magnetic pressure to gas pressure is also an important parameter. The plasma parameter β is given by:

$$\beta = \frac{8\pi P}{B^2} \tag{2.2}$$

where P is the plasma pressure and B is the magnetic field. β is generally much larger in astrophysical systems (order of hundreds or thousands) than in magnetic-confinement fusion, where β is usually around .01.

Having established some basic properties of a plasma, we can now investigate some theories to model them, starting with kinetic theory.

2.1.2 Vlasov Kinetic Theory

Kinetic theory generalizes the brute-force method of applying Maxwell's equations (and the Lorentz Force Law) to many particles. The main result, known as the Vlasov equation, is:

$$\frac{\partial f_s(\vec{x}, \vec{v}, t)}{\partial t} + \vec{u}_k \frac{\partial f_s}{\partial x_k} + \frac{q}{m} \left(\vec{E} + \frac{\vec{v}}{c} \times \vec{B} \right)_k \frac{\partial f_s}{\partial v_k} = C[f_s] \tag{2.3}$$

where f_s is the phase-space density, or distribution function, which depends on the phase-space coordinates $\vec{x}$ and $\vec{v}$. In contrast, $\vec{u}_k$ is the velocity of particle k with charge q and mass m in electric and magnetic fields $\vec{E}$ and $\vec{B}$. The left side depends only smoothly-varying terms, whereas the right is spiky, being the average of products of delta functions. The righthand side represents the interactions between individuals particles, and we can lump all these effects into the so-called "collision operator" $C[f]$. Entire graduate courses can be taught on the collision operator so we will not delve too much

into it here.

We define the distribution function to be normalized such that:

$$\rho(\vec{x}, t) = \int d^3 \vec{v} f(\vec{x}, \vec{v}, t) \qquad (2.4)$$

where ρ is the mass density and we have summed over species. Conservation laws emerge by taking different moments of the Vlasov equation and the collision operator. The k-th moment is defined as taking the integral $\int d^3 v \, \vec{v}^k f_s$. Particle conservation, for example, arises from taking the zeroth-moment of the distribution function. Such moments are usually done in the frame moving with the bulk velocity of the fluid.

A problem arises, however: every conservation law involves a higher moment of the distribution function. The evolution of density involves velocity, evolution of velocity involves the pressure tensor $\vec{P}$, evolution of the pressure involves the heat flux tensor $\vec{Q}$, and so on. This pattern of always involving higher moments of the distribution function does not simply disappear. Rather, it is a central problem of plasma physics known as the BBGKY hierarchy. It is various choices to "close" this loop of higher moments that defines different theories.

Methods to close the moment equations fall broadly into three categories: truncation, cases with special values for the distribution function or stress tensor, and asymptotic methods. The most straightforward solution is to simply truncate the hierarchy: just call the heat flux tensor $\vec{Q} = 0$. This method can lead to useful intuition, but also means that the amount of error is not well-accounted for at all. There are also special cases such as having a Maxwellian distribution function (and thus assuming local thermal equilibrium) or assuming a cold plasma that eliminate the need for the fourth moment equation [55]. The last closure method is that of asymptotics. This method generally assumes an ordering of certain parameters and expands about small values; which parameters are large or small depends on the ex-

act type of asymptotic closure. This method is thereby more rigorous and the one that leads to ideal and Braginskii MHD, discussed below.

The standard so-called "MHD ordering" assumes a magnetized plasma and takes $\delta \to 0$. Assumptions from this point forward divide MHD into its different branches (for example, single-fluid ideal MHD and Braginskii MHD) and will be discussed in subsequent sections.

2.1.3 Single-fluid MHD

In single-fluid MHD, all species are treated as a single fluid. That is, to lowest-order they all have the same temperature and flow velocity and we average out the individual particles' positions and velocities. The important quantities are bulk variables, like the mean flow of the fluid, density, and pressure (one can already see how these variables might not make as much sense for an extremely diffuse plasma such as the weakly collisional ones described in Chapter 1).

We consider MHD with the transport coefficients η and ν, the resistivity and shear viscosity (inversely proportional to the collision frequency), respectively. Ideal MHD can be obtained by setting these numbers to zero. The full set of equations is the moment equations combined with Maxwell's equations:

$$0 = \rho \frac{\partial \vec{v}}{\partial t} + (\rho \vec{v} \cdot \nabla)\vec{v} + \nabla P - \frac{1}{4\pi}(\nabla \times \vec{B}) \times \vec{B} - \nu \left(\nabla^2 \vec{v} + \frac{1}{3}\nabla(\nabla \cdot \vec{v}) \right)$$
(2.5)

$$0 = \frac{\partial \rho}{\partial t} + \nabla \cdot (\rho \vec{v})$$
(2.6)

$$0 = \frac{\partial \vec{B}}{\partial t} - \nabla \times (\vec{v} \times \vec{B} - \eta \nabla \times \vec{B})$$
(2.7)

$$0 = \frac{Dp}{Dt} + \frac{5}{3}p\nabla \cdot \vec{v}$$
(2.8)

Here, the "convective derivative" $\frac{D}{Dt} = \frac{\partial}{\partial t} + \vec{v} \cdot \nabla$, where $\vec{v}$ is the center of mass motion of the fluid. This derivative accounts for both temporal and spatial variation as a fluid element moves along with the bulk motion of the rest of the fluid. The adiabatic index γ depends on the equation of state. Isothermal evolution ($P = \rho c^2$, where c is the speed of sound) takes $\gamma = 1$. This thesis will consider adiabatic evolution with $\gamma = 5/3$, that of a monatomic ideal gas.

The moment equations are the first two equations, known respectively as the continuity and momentum equation, with Maxwell's equations slipped into the momentum equation and appearing as the induction equation (2.7). This can be seen by considering Ohm's law: $\vec{J} = \sigma(\vec{E} + \frac{1}{c}\vec{v} \times \vec{B})$, where σ is the plasma conductivity. Combining with Ampere's law $\vec{J} = \frac{c}{4\pi}\nabla \times \vec{B}$ after neglecting the displacement currents since the fluid is nonrelativistic, we have $\vec{E} = \frac{c}{4\pi\sigma}\nabla \times \vec{B} - \frac{1}{c}\vec{v} \times \vec{B}$. Now using Faraday's law, we have

$$\frac{1}{\sigma}\nabla \times \vec{J} - \frac{1}{c}\nabla \times (\vec{v} \times \vec{B}) = -\frac{1}{c}\frac{\partial B}{\partial t}$$

which leads to the induction equation after identifying $\eta = c^2/4\pi\sigma$. The other Maxwell's laws are contained in the assumption of quasi-neutrality $\sum_s n_s q_s = 0$ (Gauss's law) and by imposing the initial condition $\nabla \cdot \vec{B} = 0$, which will then remain true.

We can use a vector identity to make the separation of the magnetic field energy into two components obvious:

$$(\nabla \times \vec{B}) \times \vec{B} = (\vec{B} \cdot \nabla)\vec{B} - (\nabla\vec{B}) \cdot \vec{B} = (\vec{B} \cdot \nabla)\vec{B} - \frac{1}{2}\nabla B^2$$

where $B^2 = \vec{B} \cdot \vec{B}$. The magnetic pressure ∇B^2 term tries to increase the spacing between magnetic field lines, making the parallel with normal pressure more obvious. The magnetic tension term $-\vec{B} \cdot \nabla \vec{B}$ term tries to unfurl curves in magnetic field lines. This term plays an important role in the mechanism of accretion discussed in Chapter 3.1.2.

In ideal MHD, the magnetic field lines cannot diffuse since the plasma is perfectly conducting. This means that the field lines are effectively frozen into the plasma: the phenomenon is appropriately called "flux-freezing", or alternatively as Alfven's Theorem. Flux-freezing has important consequences for turbulence, since if a fluid particle is perturbed slightly, it will drag the magnetic field line with it. In non-ideal MHD, the field lines slip with respect to the rest of the plasma on the time scale of $\tau_R = \frac{\mu_0 L^2}{\eta}$. This time scale will become important in Chapter 3: for instance, if the dissipation time scale is shorter than characteristic time scales of the system (such as orbital time) then the magnetic field will decrease in energy, hindering the development of a magnetic dynamo.

Non-ideal MHD carries with it a number of dimensionless numbers that characterize the relative importance of various quantities. For example, the Reynolds number is given by the ratio of inertial forces to viscous forces and can be written as $\mathrm{Re} = \frac{c_0}{H} \frac{H^2}{\nu} = \frac{c_0 H}{\nu}$ where c_0 is the sound speed or other characteristic velocity in the fluid and ν is the viscosity. H is the characteristic length scale, which here we take as the scale height of the disk. Thus the Reynolds number is the amount of dissipation on disk-height length scales in one sound crossing.

The magnetic Reynolds number describes how important induction and advection of the magnetic field are compared to momentum advection of a fluid, while the ratio of the magnetic Reynolds number to the Reynolds number is called the magnetic Prandtl number:

$$\mathrm{Pm} = \frac{\mathrm{Re_M}}{\mathrm{Re}} = \frac{\nu}{\eta} \tag{2.9}$$

The magnetic Prandtl number accordingly measures how important viscous diffusion is relative to resistive diffusion. Higher magnetic Prandtl number means viscous dissipation is more important, and thus the velocity field is smoothed more than the magnetic field. In such situations we can expect

more small-scale magnetic field eddies than velocity eddies. The hydrody-namic Prandtl number measures the importance of viscosity as compared to thermal diffusion and heat conduction rather than resistivity [56].

The importance of resistivity and viscosity has been explored in a number of papers [56–58] and plays an important role in the physics of accretion, as will be discussed in Chapter 3.

Since the point of this thesis is that MHD is not valid for certain kinds of plasmas, let us now review the assumptions that went into these equations. We first assume that pressure is isotropic, which means the heat flux tensor disappears. Since we are here considering magnetized plasmas, we also take $\delta = \rho/L \to 0$. Quasi-neutrality is a good simplification since plasmas are usually overall neutral in nature. Dropping the displacement current in Ampere's law is also fine, since as mentioned earlier, the characteristic velocity of particles in our system is the thermal velocity (which is non-relativistic). Note that it is possible to include general relativity in these calculations; however, as mentioned in the introduction, this thesis is concerned with the fundamental physics, so including general relativity would be a distraction.

Lifting the requirement that pressure be isotropic and introducing a new ordering of scales leads to Braginskii MHD.

2.1.4   Braginskii MHD

Braginskii MHD uses the assumptions that the time between collisions, while not zero, is much larger than typical time scales. Equivalently, the collisional frequency is much greater than other characteristic frequencies of the system. The appropriate ordering is:

$$\rho \ll \lambda_{mfp} < L \tag{2.10}$$

Note that weakly collisional systems have mean free paths comparable to or larger than the length scales of the system: we therefore have no apparent

reason to trust Braginskii MHD in the weakly collisional regime! Such is the motivation of this thesis: we shall investigate whether we can actually accomplish a meaningful approximation.

Because the magnetic field is so strong and the gyromagnetic radius is so small compared to the mean free path, we can write the motion of particles as a sum of the guiding center motion and the gyrotropic motions about the field lines. This leads to an anisotropic pressure tensor

$$\vec{p} = \begin{pmatrix} p_\parallel & 0 & 0 \\ 0 & p_\perp & 0 \\ 0 & 0 & p_\perp \end{pmatrix} \tag{2.11}$$

if $\hat{x} = \hat{b}$ is along the magnetic field. Note that the isotropic pressure $p = \frac{2}{3}p_\perp + \frac{1}{3}p_\parallel$ and hence $p_\perp = p + \frac{1}{3}(p_\perp - p_\parallel)$ and $p_\parallel = p - \frac{2}{3}(p_\perp - p_\parallel)$.

Rigorously what follows is an expansion of the distribution function about a Maxwellian (see, e.g., [59]). However, we take a more intuitive approach here and simply argue for adding collisional terms to the evolution equations for the pressures, which arise from conservation of adiabatic invariants.

Adiabatic invariants are quantities that are "conserved" in the sense that they stay the same when changes in a system happen slowly enough. The two that we consider here are the magnetic moment μ and the mirror constant J:

$$\mu = \frac{1}{2}m\frac{w_\perp^2}{B} \qquad\qquad J \equiv m \oint w_\parallel dl$$

These are conserved as long as $\left|\frac{D\ln B}{Dt}\right| \ll \Omega$ and $\left|\frac{D\ln B}{Dt}\right| \ll \omega_b$ where ω_b is the bounce frequency associated with the magnetic mirror under consideration. Following Kunz [60], we see how these invariants relate the anisotropic

pressure and the magnetic field:

$$\langle\mu\rangle \sim \frac{p_\perp}{Bn} = \frac{T_\perp}{B} \qquad \langle J^2\rangle \sim \frac{mB^2}{n^3}p_\parallel = \frac{B^2}{n^2}T_\parallel m \qquad (2.12)$$

with $T_{\parallel,\perp} = p_{\parallel,\perp}/n$, where n is the number density instead of the mass density ρ for ease of telling p and ρ apart. An increase in the magnetic field strength will lead to an increase in perpendicular pressure, which will increase the pressure anisotropy. Combining these equations, we can come up with an equation for the evolution of the pressure anisotropy. We know that collisions push the distribution function back to a Maxwellian; therefore, we keep the pressure anisotropy small, moderated by the small parameter ω_{coll}:

$$\frac{Dp_\perp}{Dt} = p_\perp\left(\frac{D\ln Bn}{Dt}\right) - \omega_{coll}(p_\perp - p)$$
$$\frac{Dp_\parallel}{Dt} = p_\parallel\left(\frac{D\ln B^{-2}n^3}{Dt}\right) - \omega_{coll}(p_\parallel - p)$$

Subtracting these and setting the derivative of the pressure anisotropy to zero as prescribed by the Braginskii approximation, we obtain the Braginskii closure:

$$p_\perp - p_\parallel = \frac{3p}{\omega_{coll}}\frac{D}{Dt}\ln\frac{B}{n^{2/3}} = \frac{3p}{\omega_{coll}}\left(\hat{b}\hat{b} - \frac{\vec{\mathbb{I}}}{3}\right):\nabla\vec{u} \qquad (2.13)$$

The right hand side, the adiabatic invariance, produces the pressure anisotropy on the left hand side. One might conclude that, without collisions, anisotropy is produced uncontrollably. This is however not true because the adiabatic invariants are no longer conserved once certain thresholds are reached [43].

The collisionless version of this closure, known as the double-adiabatic or Chew-Goldberger-Low (CGL) closure, was originally developed for fusion devices. We shall use the Braginskii formalism because of the many problems accrued by the CGL closure in astrophysical situations [43].

We can now write the MHD equations in terms of this closure. Some work

yields:

$$0 = \frac{D \ln n}{Dt} + \nabla \cdot \vec{u} \tag{2.14}$$

$$0 = \frac{D \ln B}{Dt} - (\hat{b}\hat{b} - \vec{\mathbb{I}}) : \nabla \vec{u} \tag{2.15}$$

$$0 = \frac{3}{2} p \frac{D \ln p n^{-5/3}}{Dt} - \frac{3p}{\omega_{coll}} \left[\left(\hat{b}\hat{b} - \frac{\vec{\mathbb{I}}}{3} \right) : \nabla \vec{u} \right]^2 \tag{2.16}$$

$$0 = mn \frac{D\vec{u}}{Dt} + \nabla \left(p_\perp + \frac{B^2}{8\pi} \right) - \frac{\vec{B} \cdot \nabla \vec{B}}{4\pi} - \nabla \cdot \left[\frac{3p}{\omega_{coll}} \left(\hat{b}\hat{b} - \frac{1}{3} \vec{\mathbb{I}} \right)^2 : \nabla \vec{u} \right] \tag{2.17}$$

The right hand side of the entropy equation (2.16) in the form of $|\nabla \vec{u}|^2$ represents viscous heating. Clearly, the viscous heating is anisotropic. But what does this mean? Examining the right hand side more closely, we see that the vector $\hat{b}\hat{b} - \vec{\mathbb{I}}/3$ selects out the direction perpendicular to the magnetic field. Therefore, velocity gradients perpendicular to the magnetic field are wiped out by the dot product, whereas velocity gradients parallel to the magnetic field survive to be viscously damped. The same holds true for the momentum equation (2.17). We are led to conclude that there are no collisions across magnetic field lines, while there are collisions along magnetic field lines, leading to viscous momentum transport along field lines. Braginskii's ordering (2.10) forbids particles from moving across the field lines more than a distance of a mean free path. The situation is illustrated in Figure 2.1.

Extending this closure to the heat flux moment equation leads to anisotropic heat flux along field lines and several instabilities (including the MagnetoThermal Instability (MTI) and Heat-flux-driven Buoyancy Instability (HBI)), which have been studied both analytically and numerically for applications to the ICM and winds in hot accretion flows [60–69].
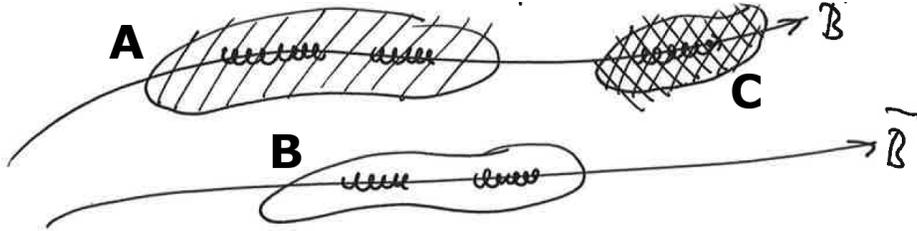
Figure 2.1: Transport of momentum along magnetic field lines $\vec{B}$. Packets of particles are shown in the blobs labelled A, B, and C. Individual particles executing Larmor motion about the field lines are also shown. Packet A can interact and collide with Packet C, but Packet B cannot interact with either Packet A or C because they lie on different field lines. From Kunz [60].

2.1.5 Kinetic effects closure

There are several approaches to modifying the fluid equations to capture kinetic effects. Sharma et al. [41] studied the transition from collisionless theory to MHD theory and found that the key difference is anisotropic collisions. This same anisotropy was present in the Braginskii MHD equations in the previous section. Braginskii MHD thus seems like an appropriate starting point off of which we can build in additional modifications to attempt to replicate kinetic effects.

Studies of kinetic theory over the years have shown that additional "parasitic" instabilities limit the growth of the pressure anisotropy in the weak field regime [38, 42]. The three most important instabilities are the firehose, mirror, and ion cyclotron instabilities. The third sets a looser limit than the mirror instability and thus will not be included [43, 70].

The thresholds for instability to the firehose and mirror instability, are respectively [38, 43, 71, 72]:

$$\frac{p_\perp}{p_\parallel} - 1 + \frac{2}{\beta_\parallel} > 0 \qquad\qquad \frac{p_\perp}{p_\parallel} - 1 < \frac{1}{\beta_\perp} \qquad (2.18)$$

These instabilities are not due to collisions since the plasma is collisionless. They are rather Alfven waves destabilized by the pressure anisotropy [43]. These waves tangle up the magnetic field of the plasma on the scale of the Larmor radius, which throws particles off of their trajectory. We can therefore model these instabilities as having an effective collision rate and thus a resistivity and viscosity [72].

In light of the thresholds above, we manually cap the pressure anisotropy over the course of our simulations in Chapter 4. The hope is that such an anisotropy maximum will sufficiently capture the kinetic instabilities in a fluid closure, as discussed in Chapter 4.

2.2 Early Problems in Accretion

The above sections have addressed the fundamental plasma physics behind radiatively-inefficient accretion flows. But how does accretion actually work on a fundamental level?

Accretion is the outward transport of angular momentum, which means that particles that lose angular momentum drop closer to the central accreting object (in the case of this thesis, a black hole) in accordance with Keplerian rotation ($\Omega(r) \sim r^{-3/2}$). It seems natural to explain this slowing down via friction; in an accretion disk, the matter at different radii are not moving at the same velocity (i.e. there is a shear) and hence one might think that there is a sort of coefficient of kinetic friction between particles that slows down their movement and causes them to accrete. The idea that this "molecular" or "shear" viscosity could explain accretion rates is tempting, but in reality is not supported by simulations or observations.

Early simulations and observations showed accretion rates on the order of $10^{15} cm^2/s$; however, the standard values of molecular viscosity are in the tens of cm^2/s, somewhere around 14 orders of magnitude too small [73]. This fantastic difference between theory and simulations resulted in several

new ideas for explaining the transport of angular momentum and led to the formulation of one of the most well-known models for thin disks—the α-disk.

The seminal paper of Shakura and Sunyaev [74] explores accretion disks in the context of a binary star system. It essentially characterizes ignorance in the accretion rate via the parameter α, defining the tangential stress $w_{r\phi} = \alpha \rho v_s^2$, where v_s is the sound speed such that $\rho v_s^2/2$ is the disk matter's thermal energy density, although definitions vary to order unity across sources [74]. This formulation provides a parameter that is easy to tweak in numerical simulations and is still in use today despite its flaws [75, 76].

Despite its intuitive usefulness, the α prescription offers no mechanism for the transport of angular momentum. It was proposed that, while pure molecular viscosity could not explain the observed accretion rates, an "effective" viscosity due to eddy interaction could do the job [76]. In other words, turbulence would generate eddies whose interactions would manifest similar to a viscosity. The problem became to find the source of the turbulence that would lead to outward angular momentum transport. Supposing that an effective viscosity generated by turbulence can explain observed and simulated accretion rates, the question becomes: what causes this turbulence?

Some, influenced by laboratory fluid mechanics, believed that the sheer property of having a high Reynolds number (huge in astrophysical flows due to the large length scales involved) satisfactorily accounted for the needed turbulence. This allows for free energy to be extracted from the shear flow. However, Keplerian flows are stable against perturbations (i.e. experience no turbulence) where shear flows are not (Rayleigh's criterion for stability is that the specific angular momentum increases radially outward). The difference is due to epicycles in Keplerian flows, which sink the energy that would otherwise devolve into prominent disturbances. A high Reynolds number is not enough to explain the necessary turbulence.

It was long thought that hydrodynamic convective instabilities could lead to

turbulence in accretion disks [77, 78]. Other possibilities include non-local effects such as waves and shocks created by tidal forces. These effects can produce accretion at rates up to $\alpha = .01$ (about an order of magnitude too low), but only in hot disks [73]. Global disk winds, of the type suggested by Blandford and Znajek [79], could also transport angular momentum. These magnetically-driven winds could theoretically sweep matter around in such a way as to account for the high accretion rates without a viscosity while also helping account for AGN jets [80]; however, the presence of these winds in all accretion disks is debated. A more universal and fundamental explanation seems more likely.

Magnetic fields were thought to serve an amplifying role in turbulence transport. That is, with pre-existing turbulence, magnetic fields would tangle and speed along the transportation of magnetic fields [74]. It was thought that the magnetic pressure and pressure due to turbulence were distinct, and that magnetic pressure would be insignificant in disk situations, or would require large magnetic fields on the order of $10^7 - 10^8$ G to balance the gravitational pressure of infalling gas [76]. The magnetic field was mainly considered to be important due to consequences of cyclotron radiation as a cooling mechanism [81]. In 1991, Balbus and Hawley [82–84] closed the conceptual circle by showing that turbulence resulted directly from a weak magnetic field. Pre-existing turbulence was not needed; the entire sequence of generating turbulence and transporting turbulence and angular momentum could be derived as a result of a linear instability in the MHD equations (see Section 3.1). Numerous numerical simulations have since confirmed the important role of magnetic fields in accretion processes. The next chapter will explore this linear instability in the context of numerical simulations.

2.3   Past Work on Anisotropic Viscosity

Anisotropic viscosity has been studied in numerous previous works both analytically and numerically. The linear regime of Braginskii MHD has been studied to find the dispersion relation, growth rates, and fastest-growing

modes after some "straightforward but somewhat tedious algebra" which will not be replicated here [85, 86]. Stability of such disks has also been investigated [87]. The nonlinear regime of turbulence, of interest in this thesis, must be studied numerically and has already been done so in the context of the magnetothermal instability [88].

The idea of using pressure anisotropy limiters comes from studies showing that the firehose and mirror instabilities destroy anisotropy even when finite Larmor radius effects are taken into account [89, 90]. Paper I has implemented these limiters already; however, that paper uses a different formalism, namely, kinetic-MHD, to solve for the evolution of the magnetic field. It also calculates viscosity at every step, which is more computationally intensive than just setting the viscosity to have one value (the approach taken in this thesis). However, Paper I and Paper II both use $\beta = 400$, which is what this thesis also uses for ease of comparison with both the kinetic-MHD regime (although other differences such a net-flux magnetic field prevent this comparison from being exactly parallel) and the fully-kinetic regime.

In summary, this thesis investigates the ability of an old theory (Braginskii MHD) with the pre-existing idea of pressure anisotropy limiters to approximate the new results of a more complex theory.

2.4   Codes: Athena and Pegasus

The systems under consideration in this thesis are extremely complicated and thus require the use of simulations to model on large time or length scales. Two codes are used for this purpose: one, an MHD solver, the other, a hybrid-kinetic particle-in-cell (PIC) code.

The code in use in Chapters 3 and 4 to simulate MHD systems is Athena4.2 (henceforth referred to as Athena). Athena, a response to the older code ZEUS, uses a higher-order Godunov scheme for flexibility and the constrained transport technique to ensure a divergence-free magnetic field. It is

a highly-modularized grid-based code with additions such as adaptive mesh refinement (AMR) capabilities, special relativity, and dust [44, 91]. The shearing box approximation (as explained in Section 3.1.3) has also been implemented [45]. A new version of Athena, Athena++, more easily integrates general relativity and allows for better Riemannien solvers [92, 93].

For collisionless and weakly collisional plasmas, the distribution function itself must be evolved. Such evolution is accomplished with a so-called "particle-in-cell" or PIC code. Because a fully-kinetic code usually requires compromising assumptions such as reduced speed of light or a smaller ion-to-electron mass ratio, hybrid-kinetic codes such as PEGASUS, the one used in Paper II that this thesis compares its results to in Chapter 4, are perhaps more useful. PEGASUS itself treats electrons as a massless fluid, while ions are treated kinetically. This assumption is valid since ions are much hotter than the efficiently-radiating electrons [18]. PEGASUS is a second-order accurate code that uses a three-stage predictor-predictor-corrector algorithm for integration. It also uses the constrained transport method as Athena does to enforce a divergence-less magnetic field and implements the shearing box method [71].

Chapter 3

Computational Context Through the MRI

This chapter examines the solution to the problem of accretion mentioned in Section of Chapter 2.2: the MagnetoRotational Instability (MRI). In doing so, it also presents intuition on how the magnetic field interacts in a rotating flow and how the MHD equations outlined in Chapter 2.1 actually manifest. Although some traction can be gained analytically (indeed, the instability itself arises from linear theory), this chapter will use simulations to illustrate the linear and nonlinear theory of the MRI and to introduce principles of using numerical simulations.

The MRI is fundamentally a local instability; as such, we will zoom in closely to look at a small patch of the overall accretion disk with dimensions $(H, 4H, H)$ where H is the disk scale-height (see Section 3.1.3) and examine the microphysics at work (see Figure 3.1). The local MHD equations as well as important characteristics such as which wavelengths grow the fastest (and how fast they grow) are outlined in Section 3.1. Non-ideal theory and simulations introduce important concepts such as numerical dissipation in Section 3.2.
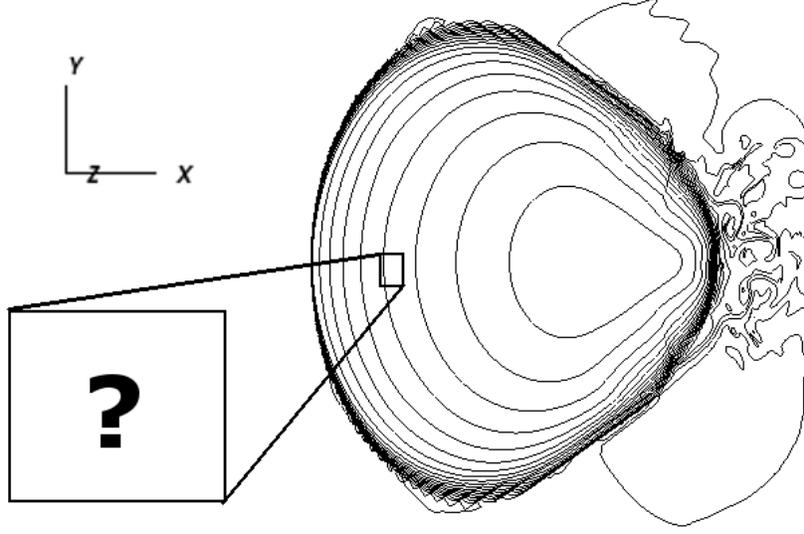
Figure 3.1: Global axisymmetric simulation of a hot accretion flow. Such simulations are expensive, so we zoom in to a small box (the "shearing box", see Section 3.1.3) to look at the microphysics.

3.1   Local Ideal MHD Theory and Simulations

In the local approximation, we consider an unperturbed patch of accretion disk with a Keplerian rotation profile at radius r_0 threaded by a uniform vertical magnetic field. On such small scales, the patch looks like a rectangular prism. We can write the equations in Cartesian form with the radial direction as x and the azimuthal direction as y. The Keplerian differential rotation in this frame looks like a combination of background shear $\vec{u}_0 = 2A_0 x \hat{y}$ (where the Oort constant $A_0 = -3\Omega_0/4$ for Keplerian flow) and the Coriolis force. The ideal MHD equations in this frame are:

$$\nabla \cdot \vec{u} = \nabla \cdot \vec{B} = 0 \tag{3.1}$$

$$\frac{\partial \vec{u}}{\partial t} = -\vec{u} \cdot \nabla \vec{u} - \frac{1}{\rho} \nabla P + \frac{1}{c\rho} \vec{J} \times \vec{B} - 2\Omega_0 \hat{z} \times \vec{u} - 4A_0 \Omega_0 x \hat{y} \tag{3.2}$$

$$\frac{\partial B}{\partial t} = \nabla \times \left(\vec{u} \times \vec{B} \right) \tag{3.3}$$

The second equation incorporates the Coriolis force $-2\Omega_0 \hat{z} \times \vec{u}$ and the background linear shear [94].

The ultimate goal here is to obtain a relationship between the frequency ω of a wave perturbation and its wavelength k. As such, we consider leading order plane-wave solutions (WKB disturbances) of the form

$$\vec{u} = 2A_0 x \hat{y} + \delta \vec{u} e^{-i(\omega t - kz)} \qquad \vec{B} = B_0 \hat{z} + \delta \vec{B} e^{-i(\omega t - kz)}$$

This form of linear theory is the cornerstone of linear instability analysis in plasma physics and can be found in a number of references [68, 76, 82–84, 94]. Plugging in this form and eliminating variables, we attain the dispersion relation

$$\omega^4 - \omega^2[\kappa^2 + 2(\vec{k} \cdot \vec{v}_A)^2] + (\vec{k} \cdot \vec{v}_A)^2 \left((\vec{k} \cdot \vec{v}_A)^2 + \frac{d\Omega^2}{d\ln R} \right) = 0 \qquad (3.4)$$

where $\vec{v}_A = \vec{B}/\sqrt{4\pi\rho}$ is the Alfven velocity. This equation is also in the Boussinesq limit that the sound speed goes to infinity, which filters out unimportant sound waves [76, 95].

3.1.1 MRI Stability and Maximum Growth Rate

From the dispersion relation Eq. 3.4, we can see the condition for stability (that is, real frequency) is

$$(\vec{k} \cdot \vec{v}_A)^2 > -\frac{d\Omega^2}{d\ln R} \qquad (3.5)$$

It is interesting to note that it is always possible to find a wavenumber k such that the system is unstable unless $\frac{d\Omega^2}{d\ln R} > 0$, which would be very uncommon in astrophysical disks [76]. Thus the MRI is always present in weakly magnetized disks with a Keplerian rotation profile.

Also note that if the magnetic field $B = 0$, then the Alfven velocity is also zero and Eq. 3.5 would have us believe that the hydrodynamic criterion

for disk stability is $\frac{d\Omega^2}{d\ln R} > 0$. We know however that the Rayleigh linear stability criterion says that $4\Omega^2 + \frac{d\Omega^2}{d\ln R} > 0$ (outwardly-decreasing specific angular momentum). The disagreement is due to the assumptions made in using the MHD equations, namely, that the mean free path of particles was much less than the length scales of interest. As k increases, we get down to such small scales that the scales of interest become comparable to the mean free path and thus this assumption is no longer valid. The conflict must be resolved through kinetic theory, which is another incentive to investigate the validity of approximating kinetic theory with MHD equations.

One of the most important questions for simulations is making sure that the wavelengths that are growing the fastest are resolved on the numerical grid. For this we need the wavelength of the fastest-growing mode, given by taking the derivative of the dispersion relation with respect to frequency. We find that the largest growth rate ω_{max} is given by

$$|\omega_{max}| = \frac{1}{2}\left|\frac{d\Omega}{d\ln R}\right| = \frac{3}{4}\Omega \qquad (3.6)$$

with the Keplerian values on the right. Plugging this back into the dispersion relation shows that the maximimum growth rate occurs when

$$(\vec{k} \cdot \vec{v}_A)^2_{max} = -\left(\frac{1}{4} + \frac{\kappa^2}{16\Omega^2}\right)\frac{d\Omega^2}{d\ln R} = \frac{15}{16}\Omega^2 \qquad (3.7)$$

There are several interesting things to note here. First, the maximum growth rate is independent of the magnetic field strength or geometry. It is also very large and apparently can grow without bound (although as we will show later other instabilities keep it in check). In fact, Balbus and Hawley [96] suggest that this growth rate is the fastest possible for a linear instability that is powered by the free energy of differential rotation. The fastest-growing wavelength does not change when resistivity is added [76].

We can see this growth in action by examining Figure 3.2, which plots perturbations in azimuthal angular momentum for a small patch of the accretion disk (see Section 3.1.3). There is clearly a periodic structure which
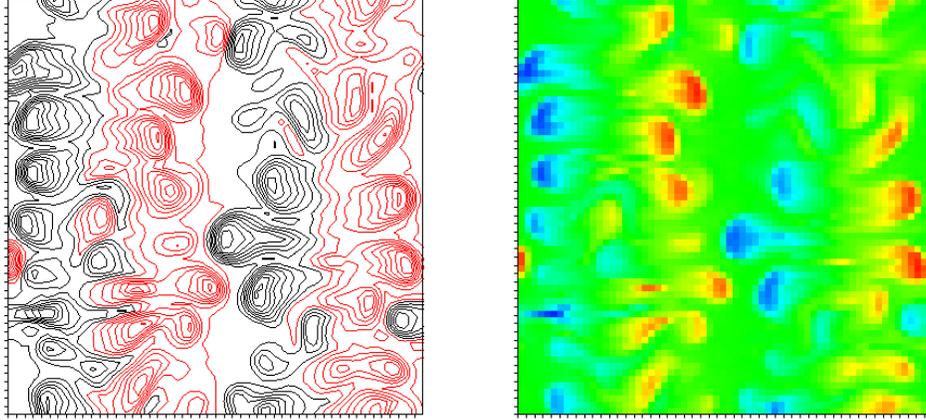
Figure 3.2: Slice at $t = 3.0$ orbits. Central body is on the left; z-direction is up. Plots are normalized to initial pressure. Left: Contour plot of twenty azimuthal angular momentum perturbation levels. Black is a perturbation in the negative y-direction (which means falling radially in), while red is in the positive y-direction. Right: Pseudocolor plot of azimuthal angular momentum perturbations. The growth of the x-direction mode with wavelength .5H is clear. Also see Section 3.1.3.
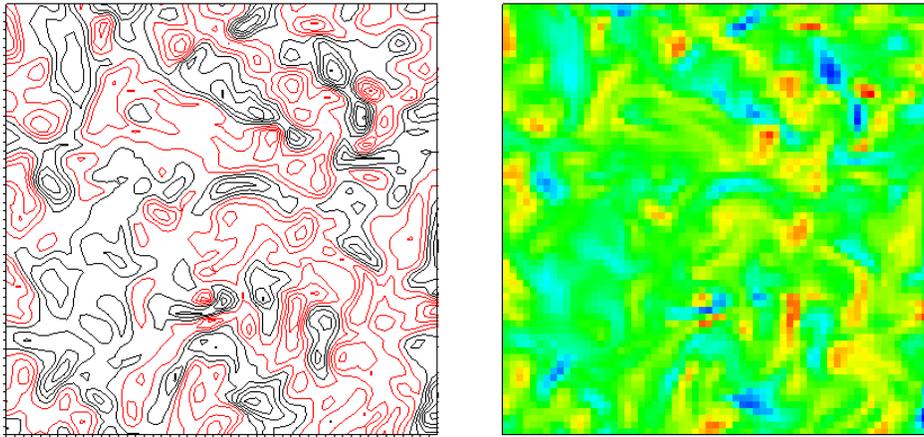
Figure 3.3: Slice at $t = 4.9$ orbits of azimuthal angular momentum perturbations (see Fig. 3.2). The system has proceeded to the nonlinear turbulence phase as evidenced by the lack of structure. Also see Section 3.1.3.

in the x-direction has a wavelength of about half of the box size. This is what we expect from Eq. 3.7:

$$(\vec{k}_{max} \cdot \vec{v}_A)^2 = k_{max}^2 \frac{B^2}{4\pi\rho} = \frac{k_{max}^2}{4\pi\rho} \frac{8\pi P}{\beta} = \frac{2P}{\beta\rho} k_{max}^2 = \frac{15}{16}\Omega^2$$

With the parameters of the simulation having been chosen to set $\Omega = 1$, $P/\rho = 1$, and $\beta = 400$, we have $k_{max} = 13.7\ H^{-1}$ in units of the computational box size H. The wavelength of the fastest growing mode is then $\lambda_{max} = .46H$. Figure 3.2 shows this and its orientation along the x-direction. The z-direction mode has a different growth rate and wavelength. In all simulations in this thesis, the magnetic field is given as $\vec{B} = B_0 \sin\left(\frac{2\pi x}{H}\right)\hat{z}$. This choice is significant only in that it has zero net flux; the actual form as a sine wave is somewhat arbitrary as it is just a simple way to achieve zero net flux.

More detailed analysis of the instability can be found in Balbus and Hawley [76, 82], Hawley and Balbus [83, 84], the last of which will henceforth be referred to as BH. The instability is different given different initial configurations of the magnetic field, the most important being the aforementioned zero net-flux condition. A radial magnetic field component will yield a time-dependent azimuthal magnetic field component; however, this dependency does not really affect the MRI evolution because the axisymmetric instability is independent of B_ϕ [76].

The magnetic energy and kinetic energy increase when the MRI is in action because some of the (in this case, unlimited) energy from Keplerian rotation is going into turbulence, sustaining the magnetic field and churning around particles. The linear phase of the MRI in Figure 3.2 gives way to turbulence shortly thereafter, as shown in Figure 3.3. The nonlinear regime is the steady-state solution and is what we are most interested in for this thesis. This is the regime that is difficult to describe analytically. The "channel mode" bump that dominates in two dimensions [82] breaks down much faster in three dimensions [97, 98], as seen in Section 3.2.

3.1.2 Spring Interpretation

It turns out that the local equations are also those of two orbiting masses coupled by a spring. A more complete derivation is given in BH, so here we only provide the physical intuition for how the MRI leads to accretion.

The situation is illustrated in Figure 3.4. One mass (call it m_o) is orbiting at a slightly higher-radius orbit r_o thanks to a perturbation. Due to the Keplerian rotation law, this mass orbits slower than the mass m_i at lower radius r_i. This means that m_i pulls ahead of m_o, thus stretching the spring. Hooke's law exerts a force pulling the springs back together, causing the inner mass to lose angular momentum and the outer mass to gain angular momentum. This means that m_i drops down to a lower orbit while m_o pulls away, thereby stretching the spring even more. The process runs away and m_i falls inward while m_o falls outward, producing outward angular momentum transport.

Obviously there is not an actual spring connecting the two masses. The job of the spring's restoring force is done by magnetic tension $\left(\frac{1}{4\pi} (\vec{B} \cdot \nabla)\vec{B} \right)$, which tries to unfurl magnetic field lines. Due to flux-freezing, the magnetic field is distorted when the fluid elements are perturbed. The field line is drawn as a dotted orange line in Figure 3.4.

3.1.3 Shearing Box Method

The shearing box method examines a small enough region of a system that stratification and curvature can be neglected, which means that results of shearing-box simulations are applicable to a broad range of flows [99]. The shearing-box approximation solves the Cartesian set of MHD equations described above with periodic boundary conditions. The model's linear shear means that if a particle moves outward with radius, it also moves
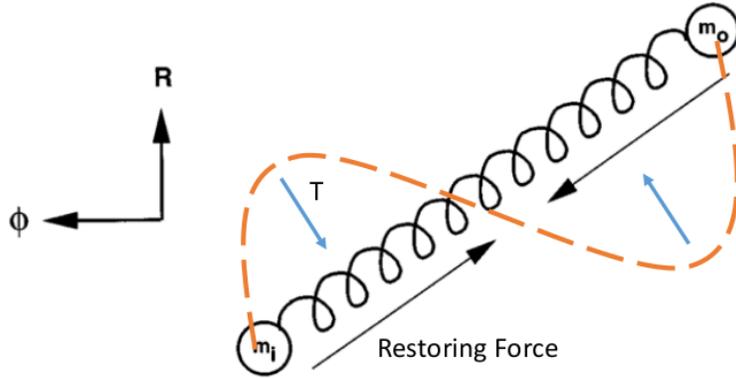
Figure 3.4: Illustration of the MRI with the magnetic tension T working in the same way as the restoring force of a spring. Adapted from BH.

azimuthally. The boundary conditions for a function f are expressed as

$$f(x, y, z) = f(x + H_x, y + \frac{3}{2}\Omega_0 H_x t, z) \tag{3.8}$$

$$f(x, y, z) = f(x, y + H_y, z) \tag{3.9}$$

$$f(x, y, z) = f(x, y, z + H_z) \tag{3.10}$$

where the first line is for the x boundary, the second for the y boundary, and the third for the z boundary. The size of the computational regime is $(H_x, H_y, H_z) = (H, 4H, H)$. A larger size in the azimuthal direction is needed because features get stretched out due to the background shear. In these equations the shear has been Taylor-expanded about the relative velocity $w_y = v_y - R\Omega_0 = R(\Omega - \Omega_0) \sim x \left(R\frac{d\Omega}{dR} \right)_0 = -\frac{3}{2}\Omega_0 x$ for a Keplerian disk. These boundary conditions are visually explained in Figure 3.5. More details can be found in BH or in the first paper simulating the MRI [84].

Since the box is in the local approximation, we can take the density and pressure to be initially constant. In this thesis, we evolve the system adiabatically as opposed to isothermally as discussed in Chapter 2.1.3. We also choose units such that the fiducial angular velocity of the shearing box as

it goes around the central body $\Omega_0 = 1$. Also choosing $P = \rho = 1$, we have that the sound speed $c = 1$ and thus that the disk height $H = 1$.

Finally, note the importance of resolution: if the fastest growing MRI mode is smaller than the size of each zone, then the simulation will not resolve the mode and the set-up will appear stable. Calling the size of each zone $(\Delta x, \Delta y, \Delta z)$, the smallest resolvable wavelength in the x-direction is

$$\lambda_{min} = 2\Delta x$$

This paper's simulations run with $(64, 128, 64)$ zones on Della and $(64, 197, 64)$ on Perseus. Each zone has a size $\Delta x = 1/64\ [H]$ and the smallest wavelength we can see corresponds to $\lambda_{min} = 1/32\ [H] \approx .03\ [H]$. We need the fastest growing wavelength to be bigger than this in order to see turbulence.
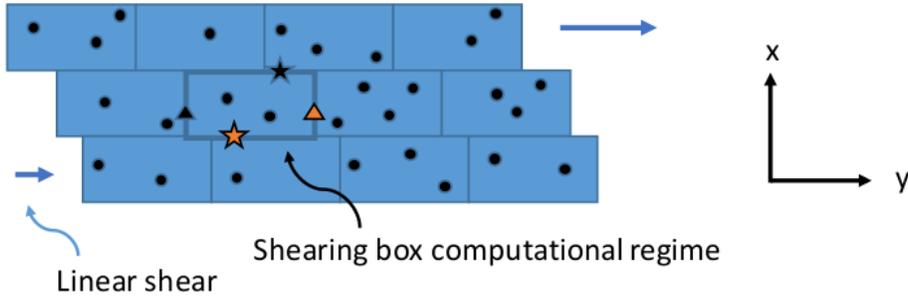
Figure 3.5: Illustration of the shearing box method. The computational regime itself is outlined in thick blue ("shearing box computational regime"). The linear shear $\vec{u}_0 = 2A_0 x\hat{y}$ is illustrated by arrows that vary in size with the x-location. A particle that travels off the right (y) boundary (orange triangle) reappears on the left y boundary at the same x-position, represented by the black triangle. The x boundary condition takes into account the linear shear, such that the orange star leaving through the x boundary reappars displaced as though by a shear at the top of the regime (black star). Adapted from BH.

3.2 Local Non-ideal MHD Theory and Simulations

This section is particularly relevant for the next chapter and understanding the effects of changing resistivity and viscosity in a fluid model. When we introduce non-ideal MHD components such as resistivity and viscosity, the resolution of simulations becomes even more important. This is because certain length scales are damped faster than others. A problem in the literature involving the lack of convergence for zero net-flux simulations such as these was recently resolved [99–101]. These papers found that in order to sustain turbulence, the box size must be larger in the vertical direction. Since the box size of this thesis is smaller in the vertical direction, we can expect some wavelengths to be cut off and therefore a minimum magnetic Prandtl number of 4 is required to sustain turbulence [56, 102] (the case is different for net-flux simulations [103]).

As a rough estimate, resistivity has a characteristic wavelength $k^2\eta \sim \Omega$ that is damped by $1/e$ over the time it takes for a sound wave to traverse the disk. Too big a value will damp the MRI and stabilize the disk [104]. Viscosity similarly damps wave numbers $k^2\nu \sim \Omega$. The balance between these two competing scales means that there is a limited parameter space in magnetic Prandtl number that can be explored. Requiring that the resistivity be large enough to damp the smallest resolvable wavelength and small enough not to damp the fastest-growing mode leads to a possible range of resistivities

$$2.5 \times 10^{-5} < \eta < 5 \times 10^{-3}$$

The same bound applies for the viscous transport coefficient ν.

A set of simulations with $\eta = 1 \times 10^{-4}$ is shown in Figure 3.6a) with varying magnetic Prandtl number. We can see that magnetic energy increases with increasing Pm. However, Figure 3.6b) shows that increasing Pm does not monotonically lead to increasing magnetic energy. This decay is due to the viscous damping of more modes, since at for example $Pm = 12$, $\nu = 24 \times 10^{-4}$ which is getting close to damping the fastest-growing mode.

In such cases, the flow will not be turbulent and so the magnetic energy will experience tranquility and decay. Note that Figure 3.6b) has a lower overall magnetic energy because the dissipation due to both resistivity and viscosity is greater.
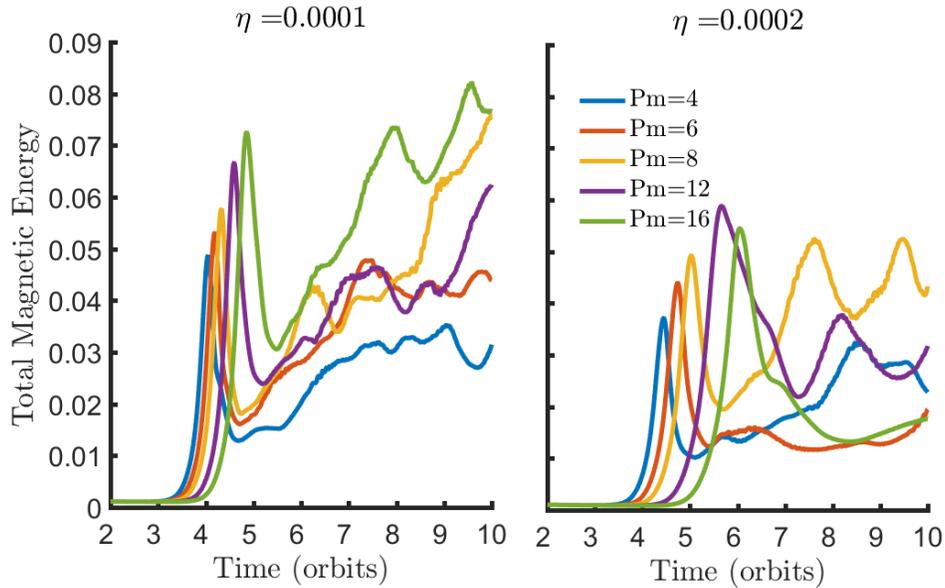
Figure 3.6: Plots of magnetic energy with increasing magnetic Prandtl number. The left panel has $\eta = 1 \times 10^{-4}$ and the right has $\eta = 2 \times 10^{-4}$. For the lower resistivity, magnetic energy increases monotonically up to $Pm = 16$. For a higher resistivity however, viscous damping begins to stabilize the MRI and higher Pm result in a decrease of magnetic energy.

Chapter 4

Modified Fluid Closure

This chapter puts together the pieces of the previous chapters in order to approximate a collisionless plasma with a modified fluid closure. The fastest-growing modes are shifted to longer wavelengths, and now instability requires

$$\lambda^2 > \frac{(2\pi v_A)^2}{3\Omega^2}\left(1 + (p_\perp - p_\parallel)\frac{4\pi}{B^2}\right) \tag{4.1}$$

As the instability grows, the fastest-growing modes may become larger than the simulation box size.

Section 4.1 explains a modification to the Athena code introduced in Chapter 2.4, while the next sections present the results of the pressure anisotropy both with and without limiters explained in Chapter 2.1.5.

4.1   Modification to Athena

The pressure anisotropy limiter was inserted manually into the code using the simplified version

$$p_\perp - p_\parallel > -\frac{B^2}{4\pi} \qquad\qquad p_\perp - p_\parallel < \frac{B^2}{8\pi}$$

We shall see later if this assumption affects the results of the simulations.

Since shearing-box simulations with anisotropic viscosity have never been done before, the publicly-available code did not work perfectly initially. The issue stemmed from using the orbital advection algorithm FARGO, which takes into account the background shear of a differentially-rotating disk to improve the efficiency and accuracy of the code. The code then solves for fluctuations on top of this background [45].

When the orbital advection algorithm is in use, the shear velocity needs to be removed from calculating the pressure anisotropy and viscous stress. The result is a simple insertion of an if statement into various places in the code, but this change dramatically impacts the output variables since the pressure anisotropy depends on the gradient of the velocity. Without the modification, the pressure anisotropy $p_\perp - p_\parallel$ is negative, which makes no sense because the perpendicular pressure should grow with increasing magnetic field. However, such a mistake did reveal that the dominant pressure anisotropy is due to the background shear.

4.2 Linear Growth

Although the main goal of this thesis is to characterize the nonlinear regime of turbulence, it is still useful to look at the linear growth of the MRI and compare the anisotropic limited and unlimited viscosity cases. Figure 4.1 plots the azimuthal angular momentum perturbations at two different times for both cases. The limiter clearly affects the evolution of the turbulence, as shown by the top row, where the angular momentum perturbations saturate in the uncapped case. At the end of ten orbits, the turbulence in the uncapped case has larger patches of material that is moving in opposite direction. This effect will be discussed further in Section 4.4.
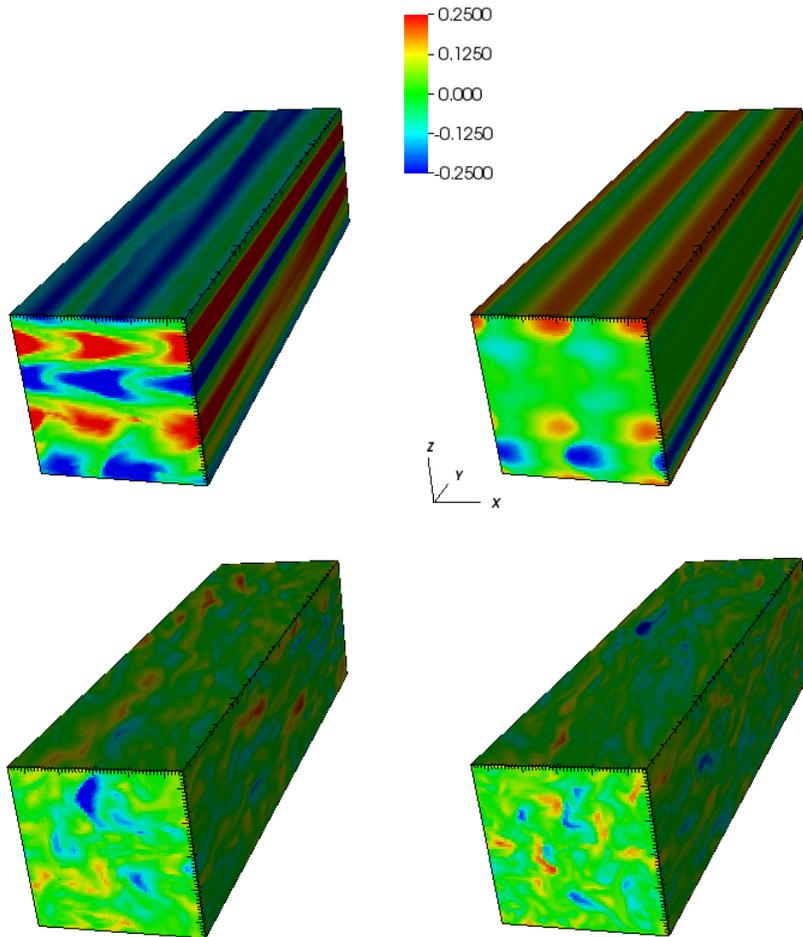
Figure 4.1: Comparison of evolution of azimuthal angular momentum perturbations for uncapped (left column) and capped (right column) anisotropy. The top row is at time $t = 3.4$ orbits and the bottom is at $t = 10.0$ orbits.

4.3 Comparison with Isotropic Viscosity

Comparing the anisotropic viscosity to the well-understood isotropic viscosity case discussed in Chapter 3 shows the complexity of anisotropic viscosity. Figure 4.2 shows the entire shearing box domain for isotropic and anisotropic viscosity. When anisotropic viscosity is enabled, the transport properties are
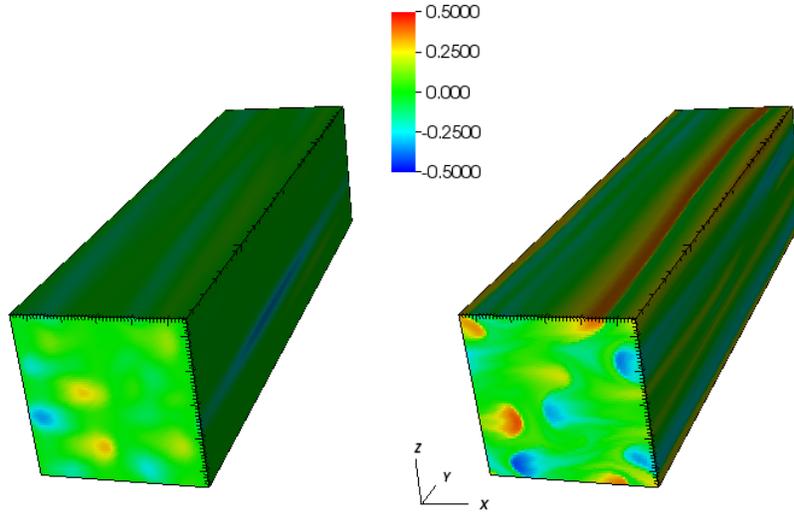
Figure 4.2: Short comparison of azimuthal angular momentum perturbations at $t = 3.5$ orbits for isotropic viscosity (left) and capped pressure anisotropy (right).

altered, as evidence by the different shapes of the modes.

Figure 4.3 compares different box-averaged quantities for isotropic viscosity and the two types of anisotropic viscosity. The isotropic viscosity magnetic energy thrives as discussed in Chapter 3.2. The channel mode is evident in all three cases and the relative importance of the different x, y, and z components also remains the same. The uncapped anisotropic viscosity, however, decays in magnetic energy while the other two grow or remain more-or-less constant. Whether a dynamo is present actually remains to be seen, since these simulations were only run for 10 orbits whereas typical simulations to determine if the dynamo is sustained run for on the order of 100 orbits. It is possible that the magnetic energy for the anisotropic viscosity will rebound. If it does not, then we must explain why the uncapped pressure anisotropy decays in magnetic energy.
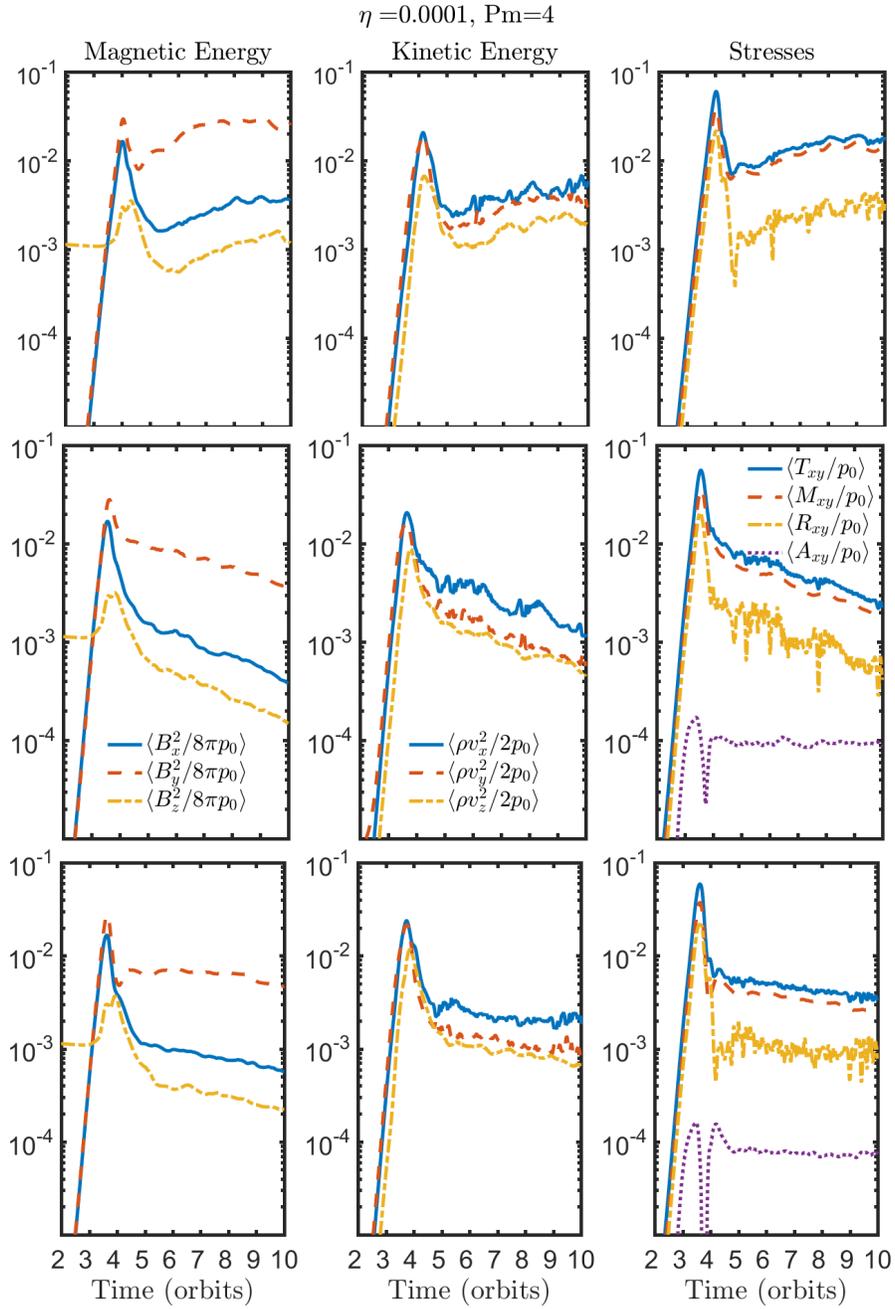
Figure 4.3: Comparison of three types of viscosity: isotropic (top), anisotropic uncapped (middle), and anisotropic capped (bottom).

If we think about anisotropic viscosity as viscosity that only acts along the magnetic field lines, then it is effectively one-third the isotropic value. Thus an isotropic magnetic Prandtl number of 4 would mean an effective magnetic Prandtl number of 4/3 in the anisotropic case. We could therefore be running into the problems of minimum (or "critical") Pm discussed in Chapter 3. Simulations with larger box size would be able to tell.

The difference between unlimited and limited pressure anisotropy can be readily explained. The anisotropy limiter keeps dissipation in check, whereas in the uncapped case it increases uncontrollably and therefore damps the magnetic activity. The same is true for kinetic energy. These results suggest that the values of $\eta = 1 \times 10^{-4}$ and $\nu = 4 \times 10^{-4}$ are appropriate for studying sustained turbulence in the anisotropy-limited case.

The stresses involved are important because the viscous stress $A_{xy} = -(p_\perp - p_\parallel)\frac{B_x B_y}{B^2}$ is what gives rise to increased angular momentum transport [38]. Figure 4.3 shows that the evolution of the total stress $T_{xy} = M_{xy} + R_{xy} + A_{xy}$ in all three cases is dominated by the Maxwell stress $M_{xy} = -\frac{B_x B_y}{4\pi}$, while the Reynolds stress $R_{xy} = \rho u_x u_y$ is about an order of magnitude lower. These values are overall about an order of magnitude lower than in Paper II, most likely due to the values of the transport coefficients. Clearly, the viscous stress with these values barely plays a role, whereas in Paper II the viscous stress is slightly below but comparable to the Maxwell stress. In order to better replicate Paper II, we need higher values of viscosity.

Figure 4.4 accordingly shows a higher value of ν for the capped and uncapped anisotropic viscosity (the isotropic viscosity's magnetic energy decays, not shown). However, both because the viscosity is only acting along one direction and the fastest-growing mode is at larger wavelengths, the magnetic energy for the anisotropic viscosity does not decay, as indicated by the flat Maxwell stress in both the capped and uncapped case. However, the viscous stress fails to surpass the Reynolds stress in terms of importance. We can attempt to fix this by looking at higher values of resistivity and viscosity.
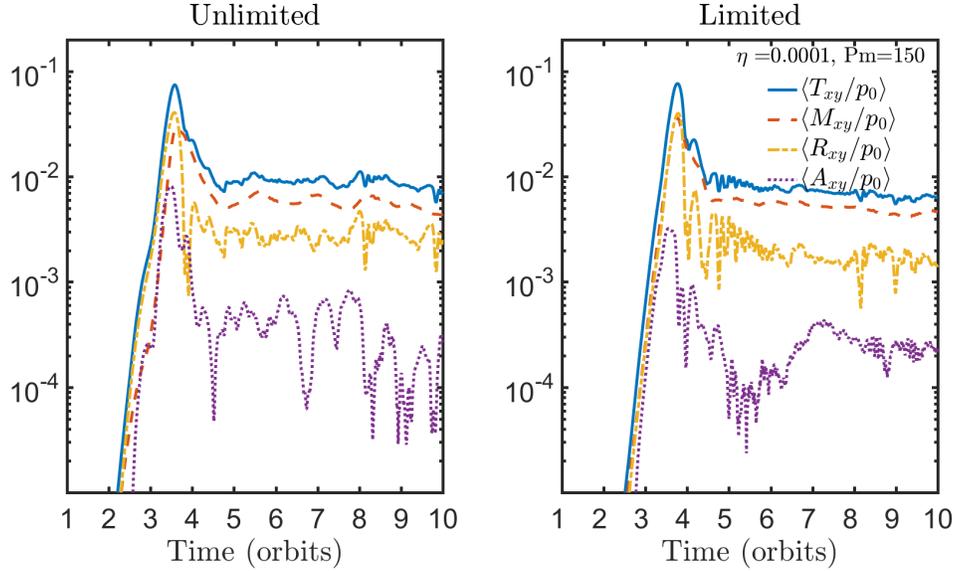
Figure 4.4: Comparison of limited and unlimited anisotropic viscosity stresses at high values of ν: here, $\nu = 1.5 \times 10^{-2}$.

Figure 4.5 shows an equivalent Pm of 150 but with the resistivity increased by a factor of two. As seen in the unlimited case, the viscous stress now rises to approximately the same order of magnitude as the Reynolds and Maxwell stress. However, the magnetic energy is decreasing in both cases, as seen by the downward-sloping Maxwell stress which of course limits the viscous stress for the capped anisotropy case. Unfortunately, higher resistivity appears not to sustain turbulence, which is needed for the MRI to transport angular momentum. The effect is even more dramatic at higher resistivity. We therefore need to keep looking at lower resistivities but at higher viscosity.

For reference and comparison to Figure 11 in Fromang et al. [56], we plot whether the magnetic energy is clearly sustained, clearly decays, or somewhere in-between (to be established with longer simulations) as a function of Reynolds number and magnetic Reynolds number in Figure 4.6. Results are also summarized in Table 4.1.
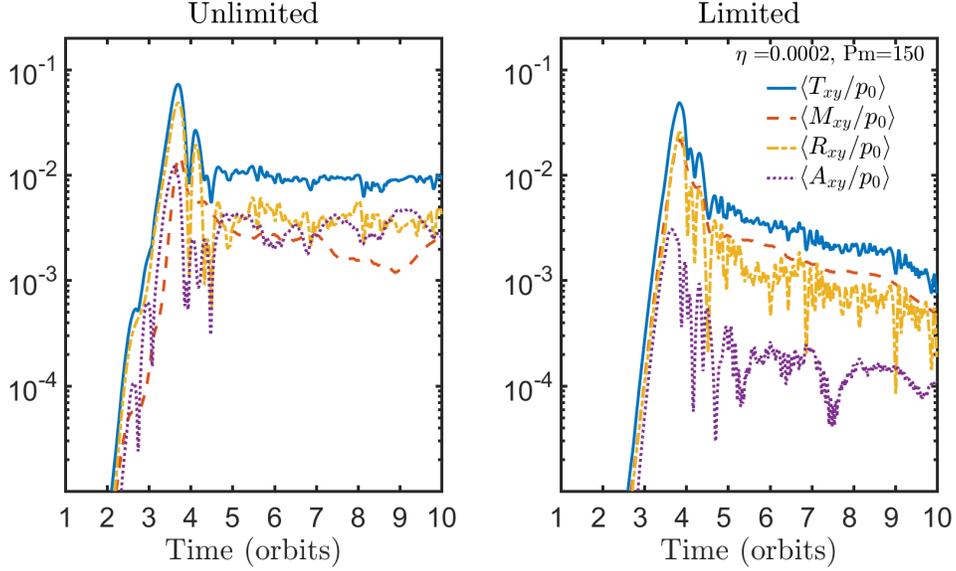
Figure 4.5: Comparison of limited and unlimited anisotropic viscosity stresses at a higher value of η: here, $\eta = 2 \times 10^{-4}$.

η/Pm	4	6	8	12	16	20	24	30	40	50	75	100	150
1×10^{-4}	Y	Y	Y	?	Y	?	?	Y	?	Y	?	?	Y
2×10^{-4}	Y	?	N	Y	Y	?	Y	?	N	N	N	N	N
3×10^{-4}	N	N	?	N	N	N	Y	?	N	?	?	N	N
4×10^{-4}	N	N	N	N	N	N	N	N	N	N	N	N	?

Table 4.1: Display of trials run and whether the magnetic energy is sustained (Y), decays (N), or is unclear (?), necessitating longer trials.

The next section will look at the distinguishing feature of the anisotropic viscosity, the pressure anisotropy, and analyze how the limiter behaves.

ReM

2500			YES
1600			YES
1250		YES	YES
500	NO	NO	YES	?
50	NO	NO	NO	YES

2500   3333   5000   10,000   **Re**
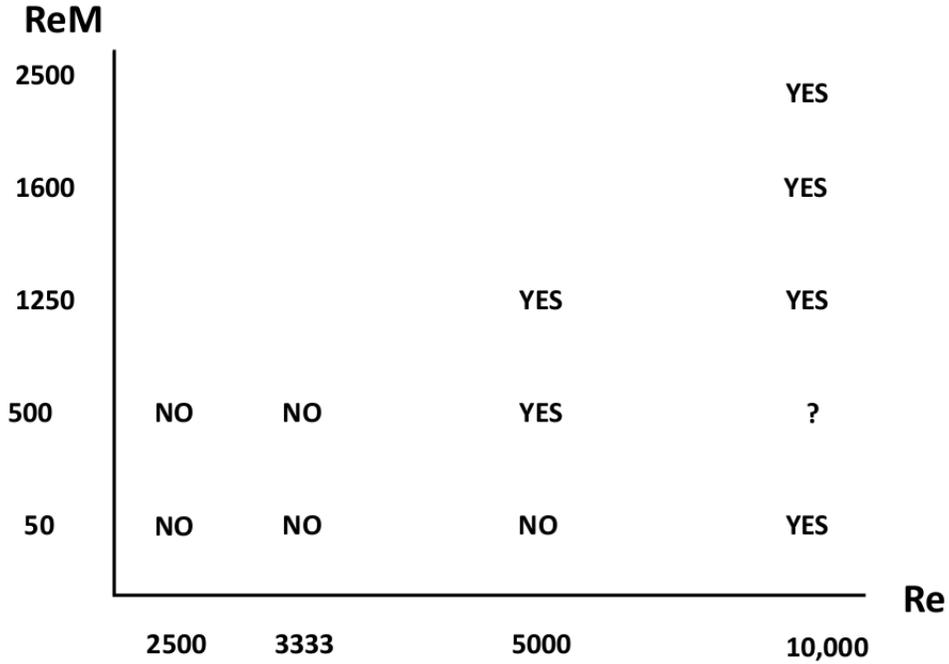
Figure 4.6: Summary of capped anisotropic viscosity's ability to sustain magnetic energy and hence turbulence, necessary for accretion. The question mark means that it is difficult to tell whether the dynamo is sustained without longer trial runs. Complements Fromang et al. [56].

4.4   Effect of the Pressure Anisotropy Limiter

The main goal of the pressure anisotropy limiter was to prevent the anisotropy from increasing beyond the mirror threshold. We can see the effect in Figure 4.7. The unlimited case has an anisotropy that exceeds the magnetic energy at early times and over the course of its evolution. The anisotropy stays around a constant value, as in Paper I's run in Figure 5. Although there are several differences between this simulation and the one in Paper I (including net flux, equation of state, and exact bounds for the mirror instability), the idea is the same. The pressure anisotropy saturates, just like the magnetic energy.
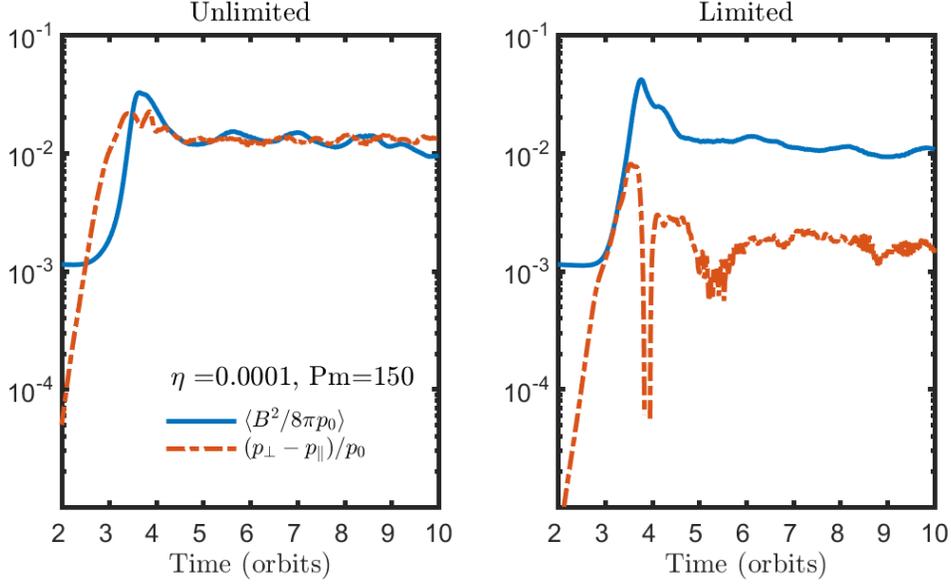
Figure 4.7: Comparison of unlimited and limited anisotropic pressure time evolution, with magnetic energy (the mirror threshold) plotted for reference.

Higher values of viscosity and resistivity exhibit this same saturation of the pressure anisotropy as seen in Figure 4.8. However, in these cases the magnetic energy decays, which significantly impacts the anisotropy-limited case but not the unlimited case. This is interesting because decreasing magnetic energy leads to an increase in parallel pressure, so even in the unlimited case one might expect to see the pressure anisotropy decrease with decreasing magnetic energy. However, since the goal of this thesis requires magnetic energy to be sustained, we shall not delve into this issue further. It might simply be a question of running the simulation for longer, since the effect is slight.

It is reassuring to see in both Figure 4.7 and Figure 4.8 that the pressure anisotropy bumps right up against the mirror threshold (which is the magnetic energy, plotted in solid blue) during the first few orbits. The limiter is clearly having an effect on the anisotropy value. However, as the unlimited
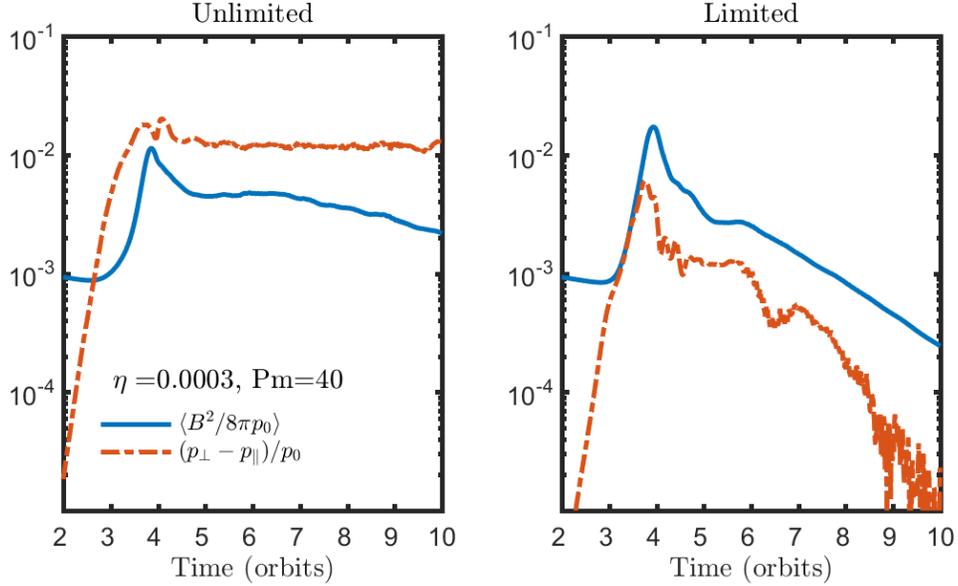
Figure 4.8: Comparison of unlimited and limited anisotropic pressure time evolution, with magnetic energy (the mirror threshold) plotted for reference.

case demonstrates, right before the channel phase is the main time when the limiter is important. This justifies our simplifying use of $\beta_\parallel$ instead of $\beta_\perp$ in the limiter equation because the two are roughly equal at that point in the evolution.

As the magnetic energy begins decreasing after the end of the channel mode, the anisotropy no longer adheres strictly to the limiter. This is because the pressure anisotropy is a volume averaged-quantity. As the magnetic field decreases, the parallel pressure increases since $p_\parallel B^2 \sim const.$ In some places of the computational domain, the pressure anisotropy is negative; that is, the pressure along the magnetic field lines exceeds the pressure perpendicular to the field lines. This can be seen explicitly in Figure 4.9, which plots the approximate pressure anisotropy throughout the domain. The fact that the pressure anisotropy is not completely positive means that the volume-averaged value will be lower than the positive-definite magnetic energy and
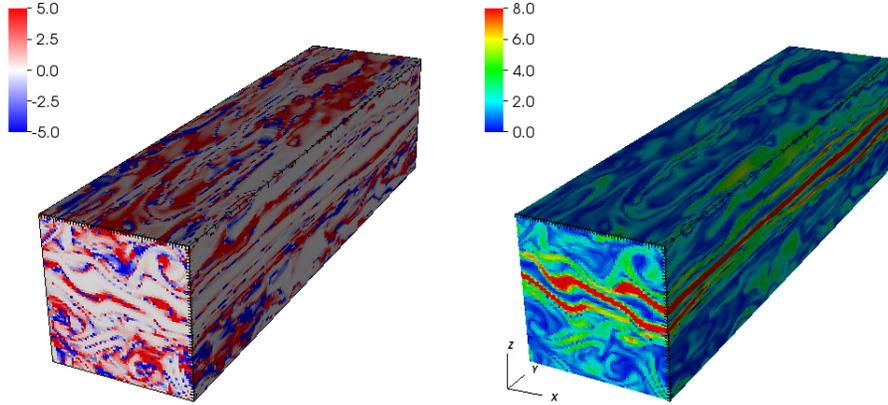
Figure 4.9: Anisotropy-limited shearing box domain during the nonlinear regime at $t = 4.1$ orbits. Left: the pressure anisotropy $p_\perp - p_\parallel$ normalized to initial pressure. Right: magnetic field strength magnitude, normalized to initial field strength.

hence there is a gap between the anisotropy and threshold values in Figures 4.7 and 4.8.

We can see the effect of the anisotropy limiter across magnetic Prandtl number in Figure 4.10, which plots selected magnetic Prandtl number trials for $\eta = 1 \times 10^{-4}$. All trials plotted have sustained magnetic energy. As already noted, lower values of viscosity do not hit the mirror threshold, whereas the effects become clearer at higher values. Larger values of resistivity exceed the mirror threshold earlier.

For completeness, Figure 4.11 shows another set of magnetic Prandtl number, demonstrating that the firehose threshold never comes into play. This is expected since the magnetic energy grows due to the MRI, and $p_\perp \sim B$. However, in trials with higher resistivity and high magnetic Prandtl number (not shown), the pressure anisotropy dips slightly negative. This might be due to the magnetic energy not being sustained, thus increasing $p_\parallel$.
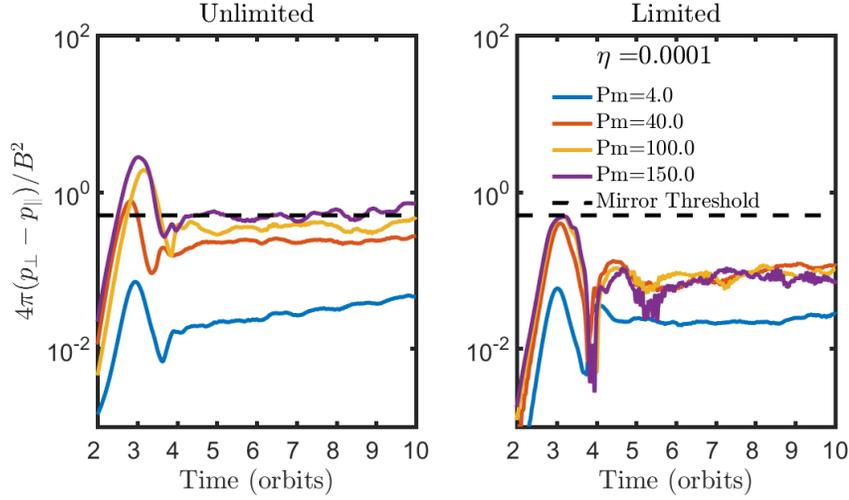
Figure 4.10: Pressure anisotropy normalized to magnetic energy, which makes it clear when the mirror threshold (dashed line) is exceeded.
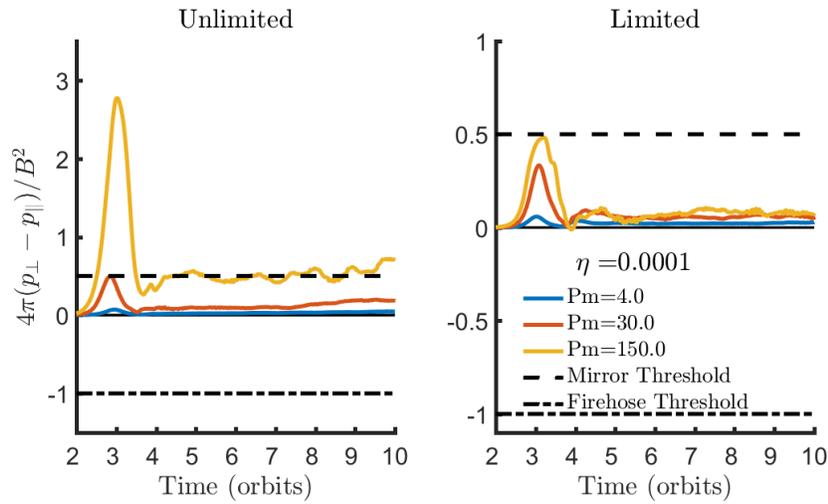
Figure 4.11: Pressure anisotropy normalized to magnetic energy, showing how the lower firehose threshold is never violated.

Chapter 5

Conclusions and Future Research

The purpose of this thesis was to find a fluid closure that approximated the physics of a weakly collisional plasma; specifically, the mirror and firehose instabilities. We have in a sense skirted the interesting parameter space, having explored resistivities from 1×10^{-4} to 4×10^{-4} with magnetic Prandtl numbers between 4 and 150, only to find that magnetic energy decayed at higher resistivity but that higher viscosity is required to reach significant levels of the viscous stress. However, such a course-grained approach was necessary in order to reveal where the interesting regimes were in the first place, since we had initially no idea what values the transport coefficients would take. Future work will fill in the gaps, both with finer values of resistivity and larger values of magnetic Prandtl number. The ambiguity of some simulations in whether their magnetic energy decays or not will also be studied by running simulations for ten times longer.

The model used in this thesis assumed spatially- and temporally-constant values of resistivity and viscosity, although the kinetic simulations of Paper II suggest a spatially-variable magnetic Prandtl number and Paper I's work suggests temporally changing the value of viscosity. This thesis knowingly simplified these aspects of Braginskii MHD; however, another regime that

would be easy to explore is the combination of anisotropic and isotropic viscosity. The interaction of both types of viscosity would have to be carefully studied before meaningful conclusions about the viscosity coefficient's profile in a weakly collisional plasma could be drawn.

The further simplification of treating the ions and electrons comprising the plasma is probably not a good one due to the difference in collision frequencies between the two species. Treating the single-fluid case is however a good starting point and recent papers have begun to extend to the two-temperature model (although in the context of general-relativistic MHD) [21].

It is somewhat ironic to note that, while one of the main motivations of this paper was to reduce the overall computation time, the numbers of cpu-hours required increases linearly with viscosity. Therefore, while magnetic Prandtl numbers of 4 are run within 32 cpu-hours, the anticipated needed magnetic Prandtl number of close to 500 will take upwards of four or five thousand. Although this amount of time is still orders of magnitude lower than the millions of cpu-hours required for PIC simulations, it still requires special permission to run for two weeks or so for a single trial (at least on Princeton computing clusters). A thorough parameter scan is thus not as computationally feasible as once thought, although it is still much less than an equivalent scan with PIC simulations and is thus still worth pursuing.

This thesis has taken a necessary step towards effectively simulating collisionless plasmas with a more computationally-manageable model, paving the way for future studies and ultimately modelling weakly collisional plasmas, including the accretion disks around supermassive black holes.

Chapter 6

Acknowledgements

Bibliography

[1] Avery E Broderick, Vincent L Fish, Sheperd S Doeleman, and Abraham Loeb. EVIDENCE FOR LOW BLACK HOLE SPIN AND PHYSICALLY MOTIVATED ACCRETION MODELS FROM MILLIMETER-VLBI OBSERVATIONS OF SAGITTARIUS A*. *Astrophys. J.*, 735(15pp), 2011. doi: 10.1088/0004-637X/735/2/110.

[2] M L Goldstein, D A Roberts, and W H Matthaeus. MAGNETOHYDRODYNAMIC TURBULENCE IN THE SOLAR WINDl. *Annu. Rev. Astron. Astrophys*, 33:283–325, 1995.

[3] W. G. Pilipp, H. Miggenrieder, M. D. Montgomery, K.-H. Muehlhaeuser, H. Rosenbauer, and R. Schwenn. Characteristics of electron velocity distribution functions in the solar wind derived from the Helios plasma experiment. *J. Geophys. Res.*, 92:1075–1092, 1987. ISSN 0148-0227. doi: 10.1029/JA092iA02p01075.

[4] M I Pudovkin and Andv S Semenov. MAGNETIC FIELD RECONNECTION THEORY AND THE SOLAR WIND -MAGNETOSPHERE INTERACTION: A REVIEW. *Sci. Rev.*, 41(1):1–89, 1985.

[5] A. Fabian. COOLING FLOWS IN CLUSTERS OF GALAXIES. *Annu. Rev. Astron ASlrophys*, 32:277–318, 1994. URL http://www.annualreviews.org/doi/pdf/10.1146/annurev.aa.32.090194.001425.

[6] C L Carilli and G B Taylor. CLUSTER MAGNETIC FIELDS. *Annu. Rev. Astron. Astrophys*, 40:319–48, 2002. doi: 10.1146/annurev.astro.40.060401.093852.

[7] P J Mendygral, T W Jones, and K Dolag. MHD SIMULATIONS OF ACTIVE GALACTIC NUCLEUS JETS IN A DYNAMIC GALAXY CLUSTER MEDIUM. *Astrophys. J.*, 750(17pp), 2012. doi: 10.1088/0004-637X/750/2/166.

[8] Matthew Kunz. Firehose and Mirror Instabilities in a Collisionless Shearing Plasma. 2010.

[9] Jason Dexter and P Chris Fragile. Tilted black hole accretion disc models of Sagittarius A*: time-variable millimetre to near-infrared emission. *MNRAS*, 432:2252–2272, 2013. doi: 10.1093/mnras/stt583.

[10] John F Hawley, Steven A Balbus, and James M Stone. A Magnetohydrodynamic Nonradiative Accretion Flow in Three Dimensions. *Astrophys. J. Lett.*, 554(1):49–52, 2001. ISSN 0004637X. doi: 10.1086/320931.

[11] James M. Stone, John F. Hawley, Charles F. Gammie, and Steven A. Balbus. Three-dimensional Magnetohydrodynamical Simulations of Vertically Stratified Accretion Disks. *Astrophys. J.*, 463(2):656, 1996. ISSN 0004-637X. doi: 10.1086/177280.

[12] Yan-Fei Jiang, James M. Stone, and Shane W. Davis. ON THE THERMAL STABILITY OF RADIATION-DOMINATED ACCRETION DISKS. *Astrophys. J.*, 778(1):65, nov 2013. ISSN 0004-637X. doi: 10.1088/0004-637X/778/1/65.

[13] Yan-Fei Jiang, James M. Stone, and Shane W. Davis. a Global Three-Dimensional Radiation Magneto-Hydrodynamic Simulation of Super-Eddington Accretion Disks. *Astrophys. J.*, 796(2):106, 2014. ISSN 1538-4357. doi: 10.1088/0004-637X/796/2/106.

[14] James; Stone and Michael Norman. Numerical Simulations of Magnetic Accretion Disks. *Astrophys. J.*, 433:746–756, 1994.

[15] N J Turner, J M Stone, and T Sano. Local Axisymmetric Simulations of Magnetorotational Instability in Radiation-dominated Accretion Disks. *Astrophys. J.*, 566(1):148–163, 2002. ISSN 0004-637X. doi: 10.1086/338081.

[16] T Sano, S-I. Inutsuka, N J Turner, and J M Stone. Angular momentum transport by MHD turbulence in accretiondisks: Gas pressure dependence of the saturation level of the magnetorotational instability. *Astrophys. J.*, 605:321–339, 2004.

[17] Ronald A Remillard and Jeffrey E Mcclintock. X-ray Properties of Black-Hole Binaries. *Annu. Rev. Astron. Astrophys.*, 44:49–92, 2006.

[18] Upasana Das and Prateek Sharma. Radiatively inefficient accretion flow simulations with cooling: implications for black hole transients. *MNRAS*, 435:2431–2444, 2013. doi: 10.1093/mnras/stt1452.

[19] Upasana Das and Prateek Sharma. Cooling and black hole disk transitions. *ASI Conf. Ser.*, 8:27–30, 2013.

[20] Andrzej Niedzwiecki, Fu-Guo Xie, and Agnieszka Stpnik. X-ray spectra of hot accretion flows. *MNRAS*, 443:1733–1747, 2014. doi: 10.1093/mnras/stu1262.

[21] Aleksander Sadowski, Jean-Pierre Lasota, Marek A. Abramowicz, and Ramesh Narayan. Energy flows in thick accretion discs and their consequences for black hole feedback. *Mon. Not. R. Astron. Soc.*, 456(4): 3915–3928, 2016. ISSN 0035-8711. doi: 10.1093/mnras/stv2854.

[22] Alexandra Veledina, Juri Poutanen, and Indrek Vurm. Hot accretion flow in black hole binaries: A link connecting X-rays to the infrared. *Mon. Not. R. Astron. Soc.*, 430(4):3196–3212, 2013. ISSN 00358711. doi: 10.1093/mnras/stt124.

[23] R.P. Fender, J. Homan, and T.M. Belloni. Jets from black hole X-ray binaries: testing, refining and extending empirical models for the coupling to X-rays. *Mon. Not. R. Astron. Soc.*, 396:1370–1382, 2009.

[24] Chris Nixon and Greg Salvesen. A physical model for state transitions in black hole X-ray binaries. *Mon. Not. R. Astron. Soc.*, 437(4):3994–3999, 2014. ISSN 00358711. doi: 10.1093/mnras/stt2215.

[25] John F Hawley, Christian Fendt, Martin Hardcastle, Elena Nokhrina, and Alexander Tchekhovskoy. Disks and Jets Gravity, Rotation and Magnetic Fields. *Sp. Sci Rev*, 191:441–469, 2015. doi: 10.1007/s11214-015-0174-7.

[26] S M Ressler, A Tchekhovskoy, E Quataert, M Chandra, and C F Gammie. Electron thermodynamics in GRMHD simulations of low-luminosity black hole accretion. *MNRAS*, 454:1848–1870, 2015. doi: 10.1093/mnras/stv2084.

[27] Feryal Oezel and Tiziana Di Matteo. X-Ray Images of Hot Accretion Flows. *Astrophys. J.*, 548:213–218, 2001.

[28] Francois Foucart, Mani Chandra, Charles F. Gammie, and Eliot Quataert. Evolution of accretion discs around a kerr black hole using extended magnetohydrodynamics. *Mon. Not. R. Astron. Soc.*, 456(2):1332–1345, 2015. ISSN 13652966. doi: 10.1093/mnras/stv2687.

[29] Avery E Broderick, Ramesh Narayan, John Kormendy, Eric S Perlman, Marcia J Rieke, and Sheperd S Doeleman. THE EVENT HORIZON OF M87. *Astrophys. J.*, 805:179, 2015. doi: 10.1088/0004-637X/805/2/179.

[30] D S Plant, R P Fender, G Ponti, T Muñoz-Darias, and M Coriat. Revealing accretion on to black holes: X-ray reflection throughout three outbursts of GX 339-4. *MNRAS*, 442:1767–1785, 2014. doi: 10.1093/mnras/stu867.

[31] R. Narayan, R. Mahadevan, J. Grindlay, R. Popham, and C. Gammie. ADVECTION-DOMINATED ACCRETION MODEL OF SAGITTARIUS A* : EVIDENCE FOR A BLACK HOLE AT THE GALACTIC CENTER. *Astrophys. J.*, 492:554–568, 1998.

[32] Avery E Broderick, Vincent L Fish, Sheperd S Doeleman, and Abraham Loeb. ESTIMATING THE PARAMETERS OF SAGITTARIUS A*'s ACCRETION FLOW VIA MILLIMETER VLBI. *Astrophys. J.*, 697:45–54, 2009. doi: 10.1088/0004-637X/697/1/45.

[33] Feng Yuan, Eliot Quataert, and Ramesh Narayan. NONTHERMAL ELECTRONS IN RADIATIVELY INEFFICIENT ACCRETION FLOW MODELS OF SAGITTARIUS A*. *Astrophys. J.*, 598:301–312, 2003.

[34] S Doeleman, Eric Agol, Fred C Baganoff Geoffrey Bower, Avery Broderick Andrew Fabian, Paul Ho Mareki Honma Thomas Krichbaum Avi Loeb Dan Marrone NRAO, U Chicago Mark Reid Alan Rogers, Irwin Shapiro Peter Strittmatter Remo Tilanus Jonathan Weintroub Alan Whitney, and Melvyn Wright. Imaging an Event Horizon: submm-VLBI of a Super Massive Black Hole. *astro 2010 Decad. Rev. Comm.*, 2009.

[35] J.P. Luminet. Black Hole Imaging (2): Heads and Tails, 2015. URL http://blogs.futura-sciences.com/e-luminet/tag/accretion-disk/.

[36] A. Siemiginowska and M. Weiss. GB1508+5714: Most Distant X-ray Jet yet Discovered, 2003. URL http://chandra.harvard.edu/photo/2003/gb1508/.

[37] J. Stone, M. Kunz, and A. Bhattacharjee. AST 521 Problem Set 1, 2016.

[38] Matthew W Kunz, James M Stone, and Eliot Quataert. Magnetorotational Turbulence and Dynamo in a Collisionless Plasma. *Phys. Rev. Lett.*, 117, 2016. doi: 10.1103/PhysRevLett.117.235101.

[39] P. Sharma, G. Hammett, and E. Quataert. Collisional Effects on the Kinetic MRI. *ASP Conf. Ser.*, 311:139–140, 2004.

[40] Prateek Sharma, Eliot Quataert, Gregory W Hammett, and James M Stone. ELECTRON HEATING IN HOT ACCRETION FLOWS. *Astrophys. J.*, 667:714–723, 2007.

[41] P. Sharma, G. Hammett, and E. Quataert. Transition from Collisionless to collisional magnetorotational instability. *Astrophys. J.*, 596:1121–1130, 2003.

[42] Prateek Sharma. Kinetic Effects on Turbulence Driven by the Magnetorotational Instability in Black Hole Accretion. *PhD Thesis, 2007*, (September), 2007.

[43] Prateek Sharma, Gregory W Hammett, Eliot Quataert, and James M Stone. SHEARING BOX SIMULATIONS OF THE MRI IN A COLLISIONLESS PLASMA. *Astrophys. J.*, 637:952–967, 2006.

[44] J. M. Stone, T. a. Gardiner, P. Teuben, J. F. Hawley, and J. B. Simon. Athena: A New Code for Astrophysical MHD. *Astrophys. J. Suppl. Ser.*, 178:137–177, 2008. ISSN 0067-0049. doi: 10.1086/588755.

[45] James M Stone and Thomas A Gardiner. IMPLEMENTATION OF THE SHEARING BOX APPROXIMATION IN ATHENA. *Astrophys. J. Suppl. Ser.*, 189:142–155, 2010. doi: 10.1088/0067-0049/189/1/142.

[46] Monika Moscibrodzka, Heino Falcke, Hotaka Shiokawa, and Charles F. Gammie. Observational appearance of inefficient accretion flows and jets in 3D GRMHD simulations: Application to Sagittarius A*. *Astron. Astrophys.*, 570, 2014. ISSN 0004-6361. doi: 10.1051/0004-6361/201424358.

[47] Hotaka Shiokawa. General Relativistic MHD Simulations of Black Hole Accretion Disks: Dynamics and Radiative Properties, 2013.

[48] Charles F Gammie, Jonathan C Mckinney, Gá Bor, and Tó Th. HARM: A NUMERICAL SCHEME FOR GENERAL RELATIVISTIC MAGNETOHYDRODYNAMICS. *Astrophys. J.*, 589:444–457, 2003.

[49] Scott C Noble, Charles F Gammie, Jonathan C Mckinney, and Luca Del Zanna. PRIMITIVE VARIABLE SOLVERS FOR CONSERVATIVE GENERAL RELATIVISTIC MAGNETOHYDRODYNAMICS. *Astrophys. J.*, 641:626–637, 2006.

[50] Scott C Noble, Julian H Krolik, and John F Hawley. DIRECT CALCULATION OF THE RADIATIVE EFFICIENCY OF AN ACCRETION DISK AROUND A BLACK HOLE. *Astrophys. J.*, 692:411–421, 2009. doi: 10.1088/0004-637X/692/1/411.

[51] Chi-Kwan Chan, Dimitrios Psaltis, Feryaï Ozel, Ramesh Narayan, and Aleksander Adowski. THE POWER OF IMAGING: CONSTRAINING THE PLASMA PROPERTIES OF GRMHD SIMULATIONS USING EHT OBSERVATIONS OF Sgr A *. *Astrophys. J.*, 799(114pp), 2015. doi: 10.1088/0004-637X/799/1/1.

[52] Monika Mocibrodzka, Charles F Gammie, Joshua C Dolence, Hotaka Shiokawa, and Po Kin Leung. RA-DIATIVE MODELS OF SGR A* FROM GRMHD SIMULATIONS. *Astrophys. J.*, 706:497–507, 2009. doi: 10.1088/0004-637X/706/1/497.

[53] G Janeschitz, P Barabaschi, G Federici, M Shimada, D J Campbell, V Mukhovatov, R Aymar, V A Chuyanov, M Huguet, and Y Shimomura. Overview of ITER-FEAT -The future international burning plasma experiment The requirements of a next step large steady state tokamak Chapter 1: Overview and summary Overview of ITER-FEAT — The future international burning plasma experiment. *Nucl. Fusion*, 41:1301–1310, 2001.

[54] G Grieger and I Milch. {D}as {F}usionsexperiment {WENDELSTEIN} 7-{X}. *Phys. Bl{ä}tter*, 49(11): 1001, 1993.

[55] R. D. (Richard D.) Hazeltine and F. Waelbroeck. *The framework of plasma physics*. Perseus Books, Reading, 2004. ISBN 9780813342139.

[56] S Fromang, J Papaloizou, G Lesur, and T Heinemann. MHD simulations of the magnetorotational insta-bility in a shearing box with zero net flux II. The effect of transport coefficients. *A&A*, 476:1123–1132, 2007. doi: 10.1051/0004-6361:20077943.

[57] G Lesur and P.-Y Longaretti. Impact of dimensionless numbers on the efficiency of magnetorotational instability induced turbulent transport. *Mon. Not. R. Astron. Soc*, 378:1471–1480, 2007. doi: 10.1111/j. 1365-2966.2007.11888.x.

[58] C. Gammie. Layered Accretion in T Tauri Disks. *Astrophys. J.*, 457:355–362, 1996.

[59] Claudia Negulescu and Stefan Possanner. CLOSURE OF THE STRONGLY MAGNETIZED ELECTRON FLUID EQUATIONS IN THE ADIABATIC REGIME. *MULTISCALE Model. SIMUL. c 2016 EUROfusion Consort.*, 14(2):839–873, 2016. doi: 10.1137/15M1027309.

[60] M. Kunz. Braginskii-MHD and application to ICM, 2016.

[61] Steven a. Balbus. Stability, Instability, and "Backward" Transport in Stratified Fluids. *Astrophys. J.*, 534 (1):420–427, 2000. ISSN 0004-637X. doi: 10.1086/308732.

[62] S. a. Balbus. Convective and Rotational Stability of a Dilute Plasma. *Astrophys. J.*, 562(2):909–917, 2001. ISSN 0004-637X. doi: 10.1086/323875.

[63] Matthew W Kunz. Dynamical stability of a thermally stratified intracluster medium with anisotropic momentum and heat transport. *Mon. Not. R. Astron. Soc*, 417:602–616, 2011. doi: 10.1111/j.1365-2966. 2011.19303.x.

[64] Ian J. Parrish and James M. Stone. Simulation of the magnetothermal instability. *Astrophys. Space Sci.*, 307(1-3):77–82, 2007. ISSN 0004640X. doi: 10.1007/s10509-006-9243-4.

[65] Ian J. Parrish and James M. Stone. Nonlinear Evolution of the Magnetothermal Instability in Two Di-mensions. *Astrophys. J.*, 633:334–348, 2005. ISSN 0004-637X. doi: 10.1086/518881.

[66] Bryan M. Johnson and Eliot Quataert. The Effects of Thermal Conduction on Radiatively Inefficient Accretion Flows. *Astrophys. J.*, 660(2):1273–1281, 2007. ISSN 0004-637X. doi: 10.1086/513065.

[67] De Fu Bu, Mao Chun Wu, and Ye Fei Yuan. Effects of anisotropic thermal conduction on wind properties in hot accretion flow. *Mon. Not. R. Astron. Soc.*, 459(1):746–753, 2016. ISSN 13652966. doi: 10.1093/ mnras/stw723.

[68] E. Quataert. Buoyancy Instabilities in Weakly Magnetized Low Collisionality Plasmas. *Astrophys. J.*, 673 (2):758–762, 2008. ISSN 0004-637X. doi: 10.1086/525248. URL http://arxiv.org/abs/0710.5521.

[69] I. Parrish and E. Quataert. NONLINEAR SIMULATIONS OF THE HEAT-FLUX-DRIVEN BUOYANCY INSTABILITY AND ITS IMPLICATIONS FOR GALAXY CLUSTERS. *Astrophys. J.*, 677:9–12, 2008.

[70] Mario A Riquelme, Eliot Quataert, and Daniel Verscharen. PARTICLE-IN-CELL SIMULATIONS OF CONTINUOUSLY DRIVEN MIRROR AND ION CYCLOTRON INSTABILITIES IN HIGH BETA ASTROPHYSICAL AND HELIOSPHERIC PLASMAS. *Astrophys. J.*, 800:27 (17pp), 2015. doi: 10.1088/0004-637X/800/1/27.

[71] Matthew W Kunz, James M Stone, and Xue-Ning Bai. Pegasus: A new hybrid-kinetic particle-in-cell code for astrophysical plasma dynamics. *J. Comput. Phys.*, 259:154–174, 2014. doi: 10.1016/j.jcp.2013.11.035.

[72] A A Schekochihin, S C Cowley, R M Kulsrud, M S Rosin, and T Heinemann. Nonlinear Growth of Firehose and Mirror Fluctuations in Astrophysical Plasmas. *Phys. Rev. Lett.*, 100, 2008. doi: 10.1103/PhysRevLett.100.081301.

[73] H Spruit. Accretion Disks. In I. Martinez-Pais, T. Shahbaz, and J. Velazquez, editors, *Accretion Process. Astrophys.*, chapter 1, pages 1–44. Cambridge University Press, 2014.

[74] N. Shakura and R. Sunyaev. Black Holes in Binary Systems. Observational Appearance. *Astron. Astrophys.*, 24:337–355, 1973.

[75] R. F. Penna, A. Sadowski, A. K. Kulkarni, and R. Narayan. The Shakura-Sunyaev viscosity prescription with variable. *Mon. Not. R. Astron. Soc.*, 428(3):2255–2274, jan 2013. ISSN 0035-8711. doi: 10.1093/mnras/sts185.

[76] Steven A Balbus and John F Hawley. Instability, turbulence, and enhanced transport in accretion disks. *Rev. Mod. Phys.*, 70(1):1–53, 1998. ISSN 0034-6861. doi: 10.1103/RevModPhys.70.1.

[77] B Paczynski. A Model of Self-gravitating Accretion Disk. *Acta Astron.*, 28(2):91–109, 1978.

[78] James M Stone, James E Pringle, and Mitchell C Begelman. Hydrodynamical non-radiative accretion flows in two dimensions. \Mnras, 322:461–472, 1999.

[79] R.D. Blandford and R. L. Znajek. Electromagnetic extraction of energy from Kerr Black Holes. *Mon. Not. R. astr. Soc.*, 179:433–456, 1977.

[80] A. Koenigl. Self-similar models of magnetized accretion disks. *Astrophys. J.*, 342:208–223, 1989.

[81] S. Shapiro. Accretion onto Black Holes: The Emergent Radiation Spectrum. *Astrophys. J.*, 180:531–546, 1973.

[82] Steven Balbus and John Hawley. A Powerful Local Shear Instability in Weakly Magnetized Disks I. Linear Analysis. *Astrophys. J.*, 376:214–222, 1991.

[83] John Hawley and Steven Balbus. A Powerful Local Shear Instability in Weakly Magnetized Disks II. Nonlinear Evolution. *Astrophys. J.*, 376:223–233, 1991.

[84] J. Hawley and S. Balbus. A Powerful Local shear instability in weakly magnetized Disks: III. Long-Term evolution in a shearing sheet. *Astrophys. J.*, 400:595–609, 1992.

[85] Steven A Balbus. VISCOUS SHEAR INSTABILITY IN WEAKLY MAGNETIZED, DILUTE PLASMAS. *Astrophys. J.*, 616:857–864, 2004.

[86] Tanim Islam and Steven Balbus. Dynamics of the Magnetoviscous Instability. *Astrophys. J.*, 633:328–333, 2005. ISSN 0004-637X. doi: 10.1086/447762.

[87] E Quataert, T Heinemann, and A Spitkovsky. Linear instabilities driven by differential rotation in very weakly magnetized plasmas. *MNRAS*, 447:3328–3341, 2015. doi: 10.1093/mnras/stu2483.

[88] De Fu Bu, Feng Yuan, and James M. Stone. Magnetothermal and magnetorotational instabilities in hot accretion flows. *Mon. Not. R. Astron. Soc.*, 413(4):2808–2814, 2011. ISSN 00358711. doi: 10.1111/j.1365-2966.2011.18354.x.

[89] P Hellinger and H Matsumoto. New kinetic instability: Oblique Alfvén fire hose. *J. Geophys. Res.*, 105526 (1):519–10, 2000. doi: 10.1029/1999JA000297.

[90] Petr Hellinger. Comment on the linear mirror instability near the threshold. *Phys. Plasmas*, 14, 2007. doi: 10.1063/1.2768318.

[91] James M Stone. The Athena MHD Code: Extensions, Applications, and Comparisons to ZEUS. *ASP Conf. Ser.*, 406:277–286, 2009.

[92] C. White and J. Stone. *Development and application of numerical techniques for general-relativistic magnetohydrodynamics simulations of black hole accretion. - Princeton University Library Catalog*. PhD thesis, Princeton University, 2016. URL https://pulsearch.princeton.edu/catalog/10096882.

[93] Christopher J White, James M Stone, and Charles F Gammie. AN EXTENSION OF THE ATHENA++ CODE FRAMEWORK FOR GRMHD BASED ON ADVANCED RIEMANN SOLVERS AND STAGGERED-MESH CONSTRAINED TRANSPORT. *Astrophys. J. Suppl. Ser.*, 225:22 (22pp), 2016. doi: 10.3847/0067-0049/225/2/22.

[94] M. Kunz. AST 521 Homework 4, 2016.

[95] M. Kunz. Notes on the Boussinesq Approximation, 2016.

[96] Steven A. Balbus and John F. Hawley. Is the Oort A-value a universal growth rate limit for accretion disk shear instabilities? *Astrophys. J*, 392:662–666, 1992. ISSN 0004-637X. doi: 10.1086/171467.

[97] John F. Hawley, Charles F. Gammie, and Steven a. Balbus. Local Three-dimensional Magnetohydrodynamic Simulations of Accretion Disks. *Astrophys. J.*, 440:742, 1995. ISSN 0004-637X. doi: 10.1086/175311.

[98] J. Hawley, C. Gammie, and S. Balbus. Local Three-Dimensional Simulations of an accretion disk hydromagnetic dynamo. *Astrophys. J.*, 464:690–703, 1996.

[99] Justin Walker and Stanislav Boldyrev. Magnetorotational Dynamo Action in the Shearing Box. *MNRAS*, 000:0–0, 2017.

[100] S Fromang and J Papaloizou. Astrophysics MHD simulations of the magnetorotational instability in a shearing box with zero net flux I . The issue of convergence. *Astron. Astrophys.*, 1122:1113–1122, 2007.

[101] Ji-Ming Shi, James M Stone, and Chelsea X Huang. Saturation of the magnetorotational instability in the unstratified shearing box with zero net flux: convergence in taller boxes. *MNRAS*, 456:2273–2289, 2016. doi: 10.1093/mnras/stv2815.

[102] Jacob B Simon, John F Hawley, and Kris Beckwith. SIMULATIONS OF MAGNETOROTATIONAL TURBULENCE WITH A HIGHER-ORDER GODUNOV SCHEME. *Astrophys. J.*, 690:974–997, 2009. doi: 10.1088/0004-637X/690/1/974.

[103] Jacob B Simon and John F Hawley. VISCOUS AND RESISTIVE EFFECTS ON THE MAGNETOROTATIONAL INSTABILITY WITH A NET TOROIDAL FIELD. *Astrophys. J.*, 707:833–843, 2009. doi: 10.1088/0004-637X/707/1/833.

[104] Timothy P Fleming, James M Stone, and John F Hawley. THE EFFECT OF RESISTIVITY ON THE NONLINEAR STAGE OF THE MAGNETOROTATIONAL INSTABILITY IN ACCRETION DISKS. *Astrophys. J.*, 530:464–477, 2000.